

CHAPTER 8

Theoretical Studies of Interactions in Nanomaterials and Biological Systems

HARALAMBOS TZOUPIS^{a,b},
AGGELOS AVRAMOPOULOS*^a, HERIBERT REIS^a,
GEORGIOS LEONIS*^a, SERDAR DURDAGI^c,
THOMAS MAVROMOUSTAKOS^b,
GRIGORIOS MEGARIOTIS^{a,d} AND
MANTHOS G. PAPADOPOULOS*^a

^a National Hellenic Research Foundation, Department of Organic and Pharmaceutical Chemistry, 48 Vas. Konstantinou, 11635, Athens, Greece;

^b National and Kapodistrian University of Athens, Department of Chemistry, Panepistimioupolis Zographou, Athens 15771, Greece; ^c University of Calgary, Department of Biological Sciences, Institute of Biocomplexity and Informatics, 2500 University Drive, AB T2N 1N4, Calgary, Canada;

^d National Technical University of Athens, Department of Chemical Engineering, 9 Heron Polytechniou Street, 15780, Athens, Greece

*E-mail: aavram@eie.gr or gleonis@eie.com or mpapad@eie.gr

8.1 Introduction

In this article, we review some of our recent work and related articles by other authors, which deal with various aspects of nanomaterials and biological complexes and in particular, the effect of interactions on some selected properties.

RSC Nanoscience & Nanotechnology No. 25

Towards Efficient Designing of Safe Nanomaterials: Innovative Merge of Computational Approaches and Experimental Techniques

Edited by Jerzy Leszczynski and Tomasz Puzyn

© The Royal Society of Chemistry 2012

Published by the Royal Society of Chemistry, www.rsc.org

The second section deals with the electronic contribution to the (hyper)polarizabilities of Li@C_{60} and $[\text{Li@C}_{60}]^+$. These properties have been computed by employing a series of methods (e.g. UB3LYP, unrestricted Møller–Plesset second-order perturbation theory (UMP2)) and basis sets (e.g. 6-31+G*). The linear and non-linear optical (L&NLO) properties of Li@C_{60} and $[\text{Li@C}_{60}]^+$ are compared with those of C_{60} and $[\text{C}_{60}]^+$. The effect of the interaction of Li with the cage, on the properties of interest is discussed. We have also studied the L&NLO properties of Li@C_{60} as a function of the distance between the Li atom and the center of the cage. The nuclear relaxation (nr) contribution to the L&NLO properties of Li@C_{60} and $[\text{Li@C}_{60}]^+$ has also been computed. In the third section we have considered the effect of encapsulation of Sc_2 in C_{72} on the L&NLO properties of $\text{Sc}_2@\text{C}_{72}$.

The fourth section deals with the L&NLO properties of Ti@C_{28} . Some spectra of Ti@C_{28} and C_{28}H_4 have been computed: (i) the UV-Vis spectra have been calculated by employing the time-dependent density functional theory (TDDFT) method with various functionals (e.g. BLYP, B3LYP), and (ii) the IR and Raman spectra have been determined in harmonic approximation using the B3LYP and CAM-B3LYP functionals. The static diagonal components of the electronic (hyper)polarizabilities of Ti@C_{28} , C_{28} and C_{28}H_4 have been calculated by various methods (e.g. restricted open-shell Møller–Plesset second-order perturbation theory (ROMP2)). The effect of the interaction of Ti with C_{28} on the L&NLO properties is discussed. The vibrational contributions (double harmonic approximation) to the L&NLO properties of Ti@C_{28} have been also computed and analyzed.

The fifth section reviews some recent works which deal with the interaction between receptors and ligands. These interactions are important because (i) they promote our understanding of the biophysical properties of the ligand–receptor system and (ii) they are an essential tool for the design of novel inhibitors. We also discuss the interactions of two fullerene derivatives with human immunodeficiency virus type 1 aspartic protease (HIV-1 PR). The binding free energy is resolved into various contributions (e.g. electrostatic, van der Waals) by using the molecular mechanics–Poisson–Boltzmann surface area (MM–PBSA) method.

The sixth section reviews an *in silico* approach to the design of novel fullerene inhibitors for HIV-1 PR. Experimental results confirmed the theoretical predictions based on docking calculations. One of the proposed derivatives has about three times better inhibitory binding than the most active, currently available, fullerene-based inhibitor.

The seventh section considers the interactions of the enzymes cyclooxygenase-2 (COX-2) and lipoxygenase-5 (LOX-5) with 4-[(2*S*)-2-(1*H*-imidazol-1-ylmethyl)-5-oxotetrahydro-1*H*-pyrrol-1-yl]methylbenzenecarboxylic acid (MMK16) by employing molecular dynamics and molecular docking techniques. MM–PBSA calculations were also used to study the interaction of aliskiren with renin in the eighth section.

The ninth section reviews the drug–membrane interactions. Two sartans, losartan and candesartan CV-11974, have been considered. Various experi-

mental techniques have been used to study the above interactions (e.g. Raman and solid-state ^{31}P NMR spectroscopies).

8.2 Li@C60

Since the discovery of C_{60} in 1985,¹ fullerene-based materials have been extensively studied due to possible applications in nanotechnology.² Among these are the endohedral fullerenes in which an atom or a molecular unit is encapsulated inside the carbon cage. A possible use of an endohedral C_{60} compound is that it can act as a memory device; if the trapped atom could be moved inside the cage between two stable positions, the position could encode the state of the device.³

A large number of studies has been performed to explore several effects associated with the stability, structure, spectroscopy, electronic and optical properties of several endohedral fullerene derivatives. These endohedral fullerenes include many atomic as well as molecular species trapped inside carbon cages, such as metal atoms, rare gas atoms and small molecules.^{4–33} All of these studies mainly deal with the effect on the electronic structure and stability of the resulting endohedral system associated with the charge transfer and covalent interactions between the fullerene cage and the entrapped unit.

An interesting topic is the determination of the linear and non-linear optical properties of endohedral fullerenes. For this purpose three systems have been selected: the endohedral fullerenes of Li@C_{60} , $[\text{Li@C}_{60}]^+$ and $\text{Sc}_2\text{@C}_{72}$. There is experimental evidence for Li@C_{60} .³⁴ Of interest is the motion of Li inside the C_{60} cage which is associated with large amplitude vibrational motions and could induce large electronic and vibrational (hyper)polarizabilities. Whitehouse and Buckingham computed the vibrational contribution to the linear polarizability and second hyperpolarizability of the $[\text{Li@C}_{60}]^+$ cation by employing a simplified potential followed by a classical analysis to obtain temperature-dependent expressions.³⁵ Their results indicated that the vibrational contribution could be larger than the electronic one. However, a study on the vibrational polarizability of Kr@C_{60} by Pederson *et al.*,³⁶ employing the double harmonic approximation, showed that this contribution was found to be quite small compared with the electronic one.

Regarding the electronic contribution to the first (β) and second (γ) hyperpolarizabilities of the neutral Li@C_{60} , one may note the studies by Campbell *et al.*^{37,38} and Yaghobi *et al.*^{39,40} Campbell *et al.* computed the diagonal components of the first hyperpolarizability employing an uncoupled Hartree–Fock scheme with the molecular orbitals obtained from the restricted open-shell Hartree–Fock procedure. In this study, an experimental measurement of the second harmonic generation response of Li@C_{60} thin films is also reported.³⁷ In ref. 38 the diagonal components of the second hyperpolarizability are computed with the same approximation as in ref. 37. Moreover an experimental measurement of the second hyperpolarizability has also been obtained by employing the z-scan and the degenerate four-wave-mixing

(DFWM) procedures.³⁸ The authors concluded that the neutral Li@C₆₀ has a response 3–5 times larger than that of pure C₆₀.

Recently, Reis *et al.* performed a detailed study of the (hyper)polarizabilities of neutral Li@C₆₀ and its cation.⁴¹ Details on the computational procedure, the methods and the software used to compute the electronic and vibrational contributions to the (hyper) polarizabilities are given in ref. 41. The first step aimed to determine the most stable geometry arrangement. For this purpose geometry optimizations were carried out for near-C_{3v} and C_{5v} symmetries employing the same level of approximation, allowing the cage to fully relax. In the case of I_h- symmetry, the cage was slightly distorted giving a C_s optimized structure with the Li atom slightly shifted (0.015 Å) from the center of the cage. However, it is known that this does not correspond to a minimum; it is associated with four imaginary frequencies. For the two minima of near-C_{5v} and near-C_{3v} symmetry the Li atom is located at 1.5 Å from the center of cage and the symmetry reduces again to C_s. The previous results are in a semi-quantitative agreement with the findings of Zhang *et al.*⁴² The eccentric position of the trapped Li has been interpreted in terms of dispersion and repulsion interactions.⁴³ It was found that the approximate C_{3v} structure is stabilized by 3.4 kJ mol⁻¹ (1.6 kJ mol⁻¹) than the C_{5v} one, employing the UB3LYP/6-311G*(UB3LYP/6-31G) method. The energy difference between the near-I_h and near-C_{3v} symmetry structures is 56.5 kJ mol⁻¹ at the UB3LYP/6-31G level of theory. The property values we report were computed by employing the near-C_{3v} structure.

Regarding the structure of the cation [Li@C₆₀]⁺, at the near-C_{3v} symmetry optimized structure, the position of the Li atom is located at 1.4 Å from the center of the cage. However, it is noted that the cation structure is more spherical than the neutral one. For this we used the following quantity $\Delta I = ((I_x - I_y)^2 + (I_x - I_z)^2 + (I_y - I_z)^2)^{1/2}$, where I_i, i = x,y,z, corresponds to the principal component of the inertia tensor in the i-direction, with respect to the center of mass. The values of ΔI were computed as 1.4 and 31.5 g Å² mol⁻¹ for the cation and the neutral structures respectively.

The computed static electronic properties of Li@C₆₀ and [Li@C₆₀]⁺, along the dipole moment direction (z), are presented in Table 8.1.

It is noted that augmentation of the basis set with diffuse functions has a large effect on the computed properties, especially on the second hyperpolarizability. Further addition of polarization functions is less important for α_{zz} and γ_{zzzz} . However, for β_{zzz} the polarization functions seem to offset the effect of the diffuse functions. A large change of the computed hyperpolarizabilities is observed on going from the cation to the neutral. This is attributed to the additional electron in a (formerly) unoccupied orbital which is localized on the C₆₀.⁴¹

In Table 8.2 some components of the properties of Li@C₆₀, [Li@C₆₀]⁺, C₆₀⁻ and C₆₀ are shown, computed at the (U)B3LYP/6-31+G* level of theory. Our scope is to investigate the effect of the interaction on the (hyper)polarizabilities between the hypothetical non-interacting species, Li⁺+C₆₀ with

Table 8.1 The electronic contribution to the polarizability, first and second hyperpolarizability of Li@C_{60} and $[\text{Li@C}_{60}]^+$, employing a series of methods and basis sets. All the computations were performed at the (U)B3LYP/6-31G optimized geometry. The property values are in a.u.

Method	$[\text{Li@C}_{60}]^+$					
	Li@C_{60}		UMP2		B3LYP	
Property	UB3LYP	UB3LYP	UB3LYP	UMP2	B3LYP	MP2
	6-31+G	6-31+G*	6-31G	6-31G	6-31+G*	6-31G
α_{zz}	578.6	589.0	508	527	534	469
β_{zzz}	1839	1532	1540	1362	-53	-237
$\gamma_{zzzz} \times 10^{-3}$	64	66	-39	99	99	28

Table 8.2 The electronic contribution to the components of the polarizability, first and second hyperpolarizability of Li@C60, [Li@C60]⁺, [C60]⁻ and C60, calculated at the (U)B3LYP/6-31+G* level of theory. All property values are in a.u.

	<i>Li@C60</i>	<i>[Li@C60]⁺</i>	<i>C₆₀^a</i>	<i>[C₆₀]^{- b}</i>
α_{xx}	560	534	550	576
α_{yy}	590	534	550	618
α_{zz}	589	534	551	620
β_{xxy}	98			
β_{xzy}		-58		
β_{yyy}	-290	0	0	-88
β_{yxz}	-1104			
β_{zzz}	1532	-118	-11	441
β_{zxx}		-52		
β_{zyz}	514	-52		
$\gamma_{xxxx} \times 10^{-3}$	293	102	136	211
$\gamma_{yyyy} \times 10^{-3}$	-20	102	135	-46
$\gamma_{zzzz} \times 10^{-3}$	66	99	136	-86

^aStructure computed at the UB3LYP/6-31G optimized geometry of [Li@C60]⁺. ^bStructure computed at the UB3LYP/6-31G optimized geometry of Li@C60.

[Li@C60]⁺ and Li⁺+C60⁻ with [Li@C60]. The properties of Li⁺ are negligible⁴⁴ and are not presented.

It can be seen that the interaction of Li⁺ with C60⁻ or C60 leads to a small reduction of the polarizability. However, the effect of the above interaction on the second hyperpolarizability of [Li@C60]⁺ is larger.

The reduction of the polarizability components of [Li@C60]⁺ may be attributed to the contraction of the electron density caused by the attraction of the cation. It is noted that the first hyperpolarizability arises from the asymmetry of the charge distribution and is enhanced in the resulting endohedral systems.

In order to study how the lithium position in C60 affects the electric properties of Li@C60, a series of computations was performed, where we considered the property of Li@C60 as a function of the distance of Li from the center of mass of the cage (Figure 8.1). All the computations were performed by using the B3LYP/6-31+G* method and are shown in Table 8.3. Only the z component of the property tensor has been computed.

It is observed that the effect of the position of Li on the polarizability and first hyperizability of Li@C60 is moderate. However, the above effect on the second hyperpolarizability is remarkable, where a change of the sign is noted.

The static and some frequency dependent nuclear relaxation (nr) contributions to the (hyper)polarizabilities were also computed in addition to the static electronic properties. The method used to compute the values of the various components is based on geometry optimization in the presence of a field. A problem which may arise is the existence of multiple minima on the potential

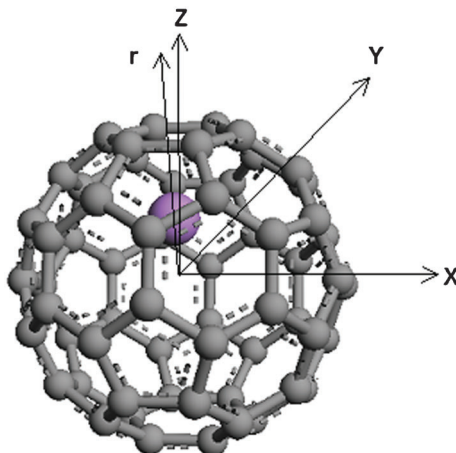


Figure 8.1 The displacement of an Li atom in the C_{60} cage.

Table 8.3 The electronic polarizability, first and second hyperpolarizability of $Li@C_{60}$ as a function of the distance between the Li atom and the centre of the cage ($r_{Li-O}/\text{\AA}$). All property values were computed with the UB3LYP/6-31+G* method and are in a.u.

r_{Li-O}	α_{zz}	β_{zzz}	$\gamma_{zzzz} \times 10^{-3}$
0	598	416	-86
0.729	594	1112	-19
0.958	593	1278	8
1.158	591	1396	32
1.358	590	1492	55
1.558	588	1569	76
2.0	584	1676	123

energy surface separated by low energy barriers. The finite-field approach works satisfactorily as long as the field-dependent optimized structure corresponds to the same minimum as the field-free one. An extensive study on this subject is presented in ref. 45. However, for the case of the studied endohedral fullerenes, it was not possible to determine the nr contribution along the x -axis and an analytical procedure was followed.⁴¹ The results of the computations are summarized in Table 8.4.

It is observed that the vibrational contributions to the polarizability components are significantly smaller than their electronic counterpart. However, the vibrational contribution to the hyperpolarizabilities is large. In particular, for the cation the x and y diagonal components are larger than the electronic ones (Table 8.2). It is also observed that the frequency-dependent nr contributions for the first hyperpolarizability connected with the dc-Pockels effect of $Li@C_{60}$ are smaller compared with the corresponding electronic ones of Table 8.2, but not negligible.

Table 8.4 The nuclear relaxation (nr) contribution to the components of the polarizability, first^a and second hyperpolarizability of Li@C60 and [Li@C60]⁺. All values were computed employing the UB3LYP/6-31G method. The property values are given in a.u.

	Li@C60	[Li@C60] ⁺
α_{xx}^{nr}	14.7	10.4
α_{yy}^{nr}	10.3	9.4
α_{zz}^{nr}	10.2	4.5
β_{yyy}^{nr}	-126	95
β_{zzz}^{nr}	795	18
$\beta_{xxz}^{\text{nr}}(-\omega; \omega, 0)_{\omega \rightarrow \infty}$	-199	
$\beta_{yyy}^{\text{nr}}(-\omega; \omega, 0)_{\omega \rightarrow \infty}$	-33	
$\beta_{yyz}^{\text{nr}}(-\omega; \omega, 0)_{\omega \rightarrow \infty}$	119	
$\beta_{zzy}^{\text{nr}}(-\omega; \omega, 0)_{\omega \rightarrow \infty}$	-9	
$\beta_{zzz}^{\text{nr}}(-\omega; \omega, 0)_{\omega \rightarrow \infty}$	200	
$\gamma_{xxxx}^{\text{nr}} \times 10^{-3}$		560
$\gamma_{yyyy}^{\text{nr}} \times 10^{-3}$	-90	190
$\gamma_{zzzz}^{\text{nr}} \times 10^{-3}$		7

^aThe frequency-dependent properties were adopted employing the infinite optical frequency approximation.⁴¹

8.3 Sc2@C72

All the properties were computed by using the fully optimized geometry. For this purpose the Hartree–Fock (HF) theory was used with the 6-31+G* basis set for C and the effective core potential for Sc developed by the Stuttgart–Dresden group.⁴⁶ This treats Sc as an atom with 11 valence electrons and the employed basis set involves *6s5p3d1f*. The computed structure is in agreement with that computed by Slanina *et al.*¹⁶ (Figure 8.2).

The shortest distance between Sc and C is 2.174 Å, in agreement with ref. 16. The two Sc atoms lie along the D_2 axis, while their interatomic distance is 4.7

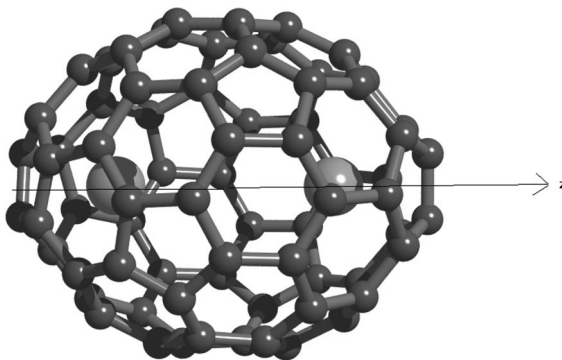


Figure 8.2 The HF optimized geometry of Sc2@C72 endohedral metallofullerene.

Å. This distance is longer than that in the isolated Sc_2 (2.28 Å, computed at the HF/6-31+G* level).

The above methodology employed for the structure optimization was used for the computation of the electronic polarizability and second hyperpolarizability of $\text{Sc}_2@C_{72}$. The usefulness of the effective core potentials for the computation of polarizabilities and hyperpolarizabilities has been discussed extensively in the literature and has been shown to provide satisfactory results for the non-linear optical (NLO) properties, compared with all-electron calculations. In order to safeguard the numerical stability of our results the Romberg fitting procedure was employed, which requires a number of computed energies, evaluated by using a number of field steps of magnitude $2^k F$, where $k = 0, 1, 2, \dots$ and $F = 0.001$ a.u. Since the two Sc atoms lie along the z -axis (D_2) we have restricted our computations to the z -component of the molecular property tensor.

It is known that vibrations play a key role on the reliable determination of the non-linear optical properties of molecules and clusters. Therefore, it is of interest to study their effect on the computed NLO properties of this metallofullerene. For this purpose the field-induced coordinate (FIC) approach has been employed.⁴⁷ With this method the total nuclear relaxation (nr) contribution to the static polarizability, and the dynamic nr contribution of the electric-field-induced second harmonic generation (EFISHG) second hyperpolarizability, were calculated. The computational scheme involves the optimization and the evaluation of a number of necessary energy and property derivatives in a numerical fashion. Details can be found in ref. 48.

All the results of the computed properties are presented in Table 8.5. It can be seen that for the polarizability the electronic (el) contribution is dominant over the vibrational one. It was found that $\alpha_{zz}^{\text{nr}} = 30.59$ a.u., which is much smaller than its electronic counterpart ($\alpha_{zz}^{\text{el}} = 749.13$ a.u.). Adopting the infinite frequency approximation, which is known to be accurate at typical measurements we found that $\gamma_{zzzz}(-2\omega; \omega, \omega, 0)_{\omega \rightarrow \infty} = 98\,800$ a.u. This value is large, but it is smaller, compared with the electronic one ($\gamma_{zzzz}^{\text{el}} = 193\,100$

Table 8.5 The electronic and nuclear relaxation contributions to the polarizability and second hyperpolarizability of $\text{Sc}_2@C_{72}$. All values are in a.u.

	<i>Electronic contribution^a</i>	<i>Nuclear relaxation contribution^b</i>
$\alpha_{zz}(0;0)$	749.13 777.41 ^b	30.59
$\gamma_{zzzz}(0;0)$	193 100 297 000 ^b	
$\gamma_{zzzz}(-2\omega; \omega, \omega, 0)_{\omega \rightarrow \infty}$	98 800	

^aAll the necessary derivatives were evaluated by employing the 6-31+G* basis function to carbon and the SDD pseudopotential to Sc. ^b C_{72} properties. The 6-31+G* basis set was used for carbon.

a.u.). It is observed that encapsulation of Sc_2 in C_{72} leads to a reduction of α_{zz} and γ_{zzzz} (Table 8.5).

1

8.4 Ti@C28

Skwara *et al.* performed an exhaustive computational study of the endohedral fullerene Ti@C28.⁴⁹ They investigated the potential energy surface, as well as its bonding properties, electronic spectra, vibrational spectra, and determined its electronic and vibrational (hyper)polarizabilities, and compared several of these properties with those of the empty fullerene C_{28} , as well as with C_{28}H_4 . The ground state of C_{28} has been predicted previously to be a quintet open shell of T_d symmetry. By contrast, the endohedral fullerene Ti@C28 as well as C_{28}H_4 are predicted to be singlets. C_{28} has been found in abundance as a product of laser vaporization of C_{60} , but appears to be very reactive. Specifically, it forms very stable endohedral complexes with tetravalent transition metals like Ti, Zr, Hf, U.

At the RMP2/6-31G(d) level, the ground state of Ti@C28 was found to be of C_{3v} symmetry, about $2.3 \text{ kcal mol}^{-1}$ below a transition state of C_{2v} symmetry, in contrast to a previous report,⁵⁰ which predicted the state of C_{2v} symmetry as the ground state, using a lower level of theory. The Ti atom in the C_{3v} structure was shifted by 0.4579 \AA along the C_3 axis, with respect to the origin in the center of nuclear charge. Additional higher-order saddle points of C_{3v} (second-order saddle point) and T_d symmetry (third-order saddle point) on the potential energy surface were found at 7.1 and $47.8 \text{ kcal mol}^{-1}$ respectively above the global minimum. Additionally to the stationary points, the interconnection of all the different stationary points on the potential energy surface was explored. The same energetic ordering of the stationary points was found at the HF and B3LYP levels of theory, using again the 6-31G(d) basis set. The equilibrium structure of C_{28} was assumed to be the 5A_2 state of T_d symmetry and computed at the RMP2/6-31(d) level. At the unrestricted Møller–Plesset second-order perturbation theory (UMP2) level, considerable spin contamination was detected. Comparison of the computed $\text{C}_{28}({}^5A_2)$ and Ti@C28(1A1) structures, as well as the $\text{Ti}({}^3F_2)$ ground state, at the R(O)MP2/6-31G(d) levels, and taking into account a Boys–Bernardi counterpoise correction, yielded a binding energy of $181.3 \text{ kcal mol}^{-1}$ for the endohedral complex, compared to literature values of $258.3 \text{ kcal mol}^{-1}$ at the LDA/VTZP⁵¹ and $-18.4 \text{ kcal mol}^{-1}$ at the HF/DZ level.⁵⁰ The large value computed indicates a strong bonding between Ti and the cage. The character of this bonding was further explored with an Atoms in Molecules (AIM) analysis, which revealed that although the four Ti...C interactions are essentially of closed-shell character, they are at the same time partially covalent.

As a next step in the characterization of Ti@C28 the UV-Vis spectrum was computed at the adiabatic TDDFT level and compared with that of the exohedral counterpart C_{28}H_4 (see Figure 8.3). For this purpose, the first 200 electronic states were determined with the BLYP, B3LYP and CAM-B3LYP

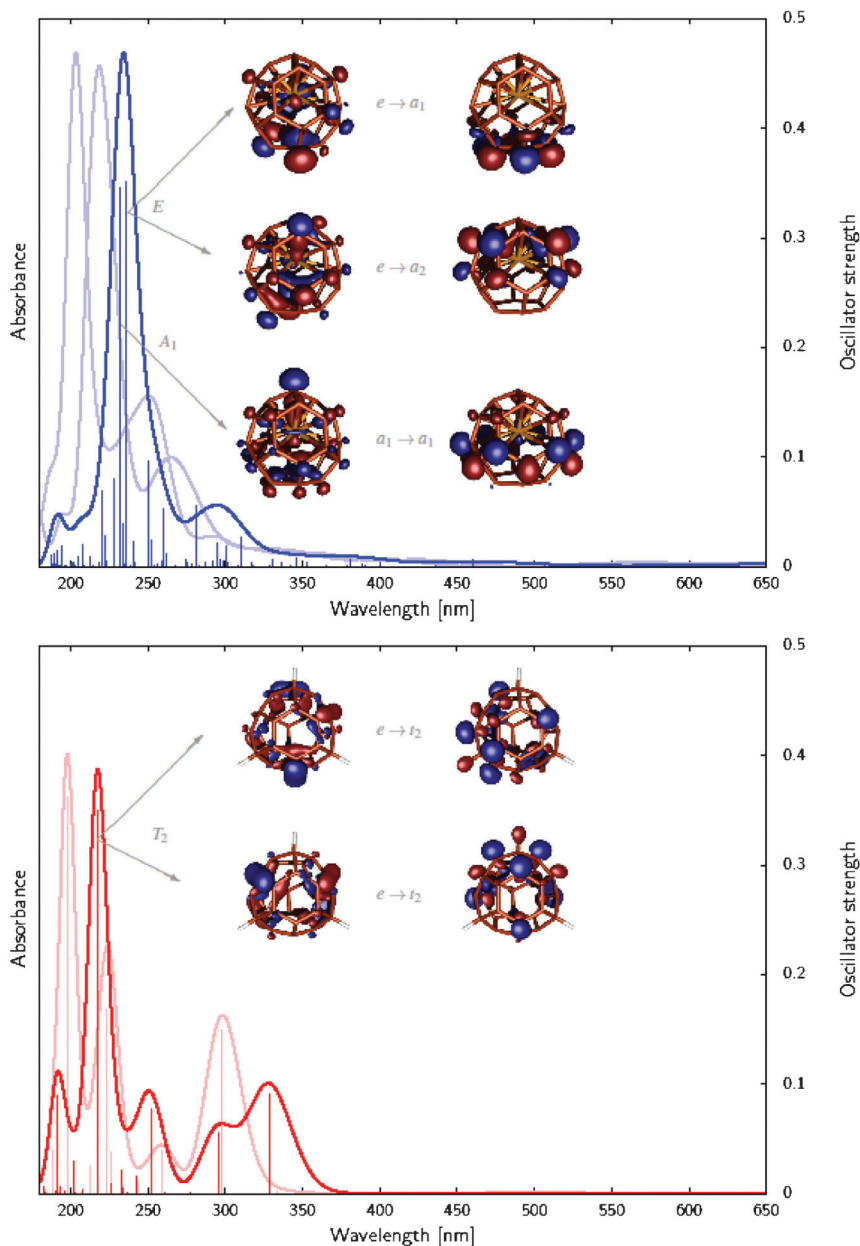


Figure 8.3 UV-Vis spectra of Ti@C₂₈ (top) and C₂₈H₄ (bottom) computed by means of the TDDFT method using BLYP (solid dark lines), B3LYP (solid light lines), and CAM-B3LYP (dashed lines, only on top figure) functionals and the 6-31+G(d) basis set. The line positions were convoluted with Gaussian functions with full widths at half-maximum of 3000 cm⁻¹. Reprinted with permission from ref. 1. Copyright (2011) American Chemical Society. 2

functionals, using the 6-31+G(d) basis set and the MP2/6-31G(d) optimized geometry. BLYP was chosen due to a previous report, which indicated that non-hybrid functionals perform reasonably well in the calculation of electronic absorption spectra of fullerenes.⁵² For the fullerenes investigated in ref. 49, it turned out that the hybrid functional B3LYP as well as the long-range-corrected functional CAM-B3LYP in fact predicted qualitatively similar absorption spectra as BLYP, with the same origin of the most intense lines, although slightly blue-shifted. Unfortunately, neither experimental spectra nor previous calculations exist for comparison.

In line with what has been found for other fullerenes, the first excited state of Ti@C₂₈, located at 650 nm and dominated by the highest occupied molecular orbital (HOMO) to lowest unoccupied molecular orbital (LUMO) transition, is dipole-forbidden and does not occur in the computed spectrum (see Figure 8.3). The same holds for most lines occurring at wavelengths above 300 nm. The most intense lines found with the BLYP functional occur at 232 nm and 236 nm and are of *A*₁ and *E* symmetry, respectively. The major contributing molecular orbitals involved in these transitions are also shown in Figure 8.3. With increasing exact exchange contribution, the most intense lines are blue-shifted by 20 nm (B3LYP) and 35 nm (CAM-B3LYP).

Comparison of the Ti@C₂₈ spectrum with that of the exohedral C₂₈H₄ reveals the influence of the Ti encapsulation on the electronic absorption spectrum. In general, both spectra are quite similar, with the main difference being that the two high-intensity lines of the Ti@C₂₈ spectrum merge into one single line of *T*₂ symmetry which, in addition, is blue-shifted (by 217 nm and 198 nm with BLYP and B3LYP, respectively). It is argued that the main effect of Ti encapsulation is the redshift of the largest peak, accompanied by an intensity increase of *ca.* 20%.

In addition to the electronic absorption spectra, IR and Raman spectra of Ti@C₂₈ and C₂₈H₄ were also computed at the harmonic oscillator level using both the B3LYP and CAM-B3LYP functionals, together with the 6-31+G(d) basis set. Figure 8.4 shows the resulting spectra after convolution of each line with a Lorentzian with a full width at half-maximum of 10 cm⁻¹. Previous researchers^{53–55} reported that B3LYP in combination with a basis set containing both diffused and polarized functions performs quite well for vibrational frequencies, IR and Raman intensities, compared with experiment and/or high-level *ab initio* calculations. Thus, a reasonably good accuracy is also assumed for the corresponding properties of Ti@C₂₈ and C₂₈H₄ reported in ref. 49, for which again no experimental values are available for comparison. The most relevant difference between the vibrational features of Ti@C₂₈ and C₂₈H₄ with respect to the electric properties is a low-frequency doubly-degenerate vibration of the former, associated with large displacements of the Ti atom inside the cage.

The non-zero diagonal electronic contributions to the electrical properties (dipole, polarizability, first and second hyperpolarizabilities) of Ti@C₂₈, C₂₈, and C₂₈H₄ calculated at the R(O)HF and R(O)MP2 levels of theory with the 6-

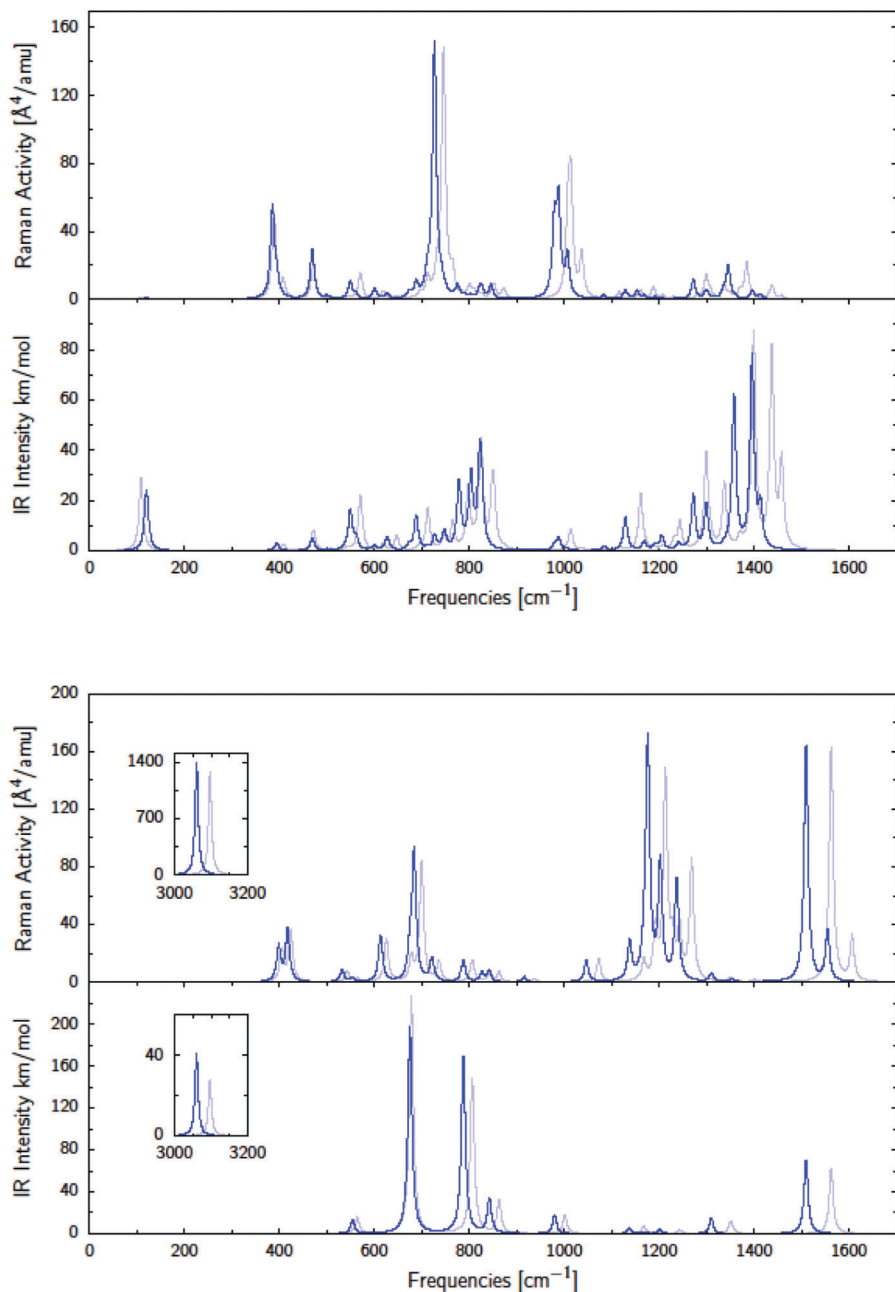


Figure 8.4 IR and Raman spectra of Ti@C₂₈ (top) and C₂₈H₄ (bottom) in harmonic approximation using B3LYP (dark blue lines) and CAM-B3LYP (light blue lines) functionals and the 6-31+G(d) basis set. This insets show the C–H stretching bands above 3000 cm⁻¹, which are present only in C₂₈H₄. Reprinted with permission from ref. 1. Copyright (2011) American Chemical Society.

Table 8.6 Static diagonal components of the electronic dipole and (hyper)polarizabilities of Ti@C₂₈, C₂₈H₄ and C₂₈ (with the cage geometry corresponding to the removal of Ti from Ti@C₂₈).

	<i>Ti@C28</i>		<i>C28 (C3v)</i>		<i>C28H4</i>	
	<i>RHF</i>	<i>ROMP2</i>	<i>ROHF</i>	<i>ROMP2</i>	<i>RHF</i>	<i>RMP2</i>
μ_z	1.612	1.088	-0.0009	-0.055	0.0	0.0
α_{xx}	267.20	275.96	254.92	277.40	246.59	251.06
α_{zz}	245.81	258.83	258.94	281.04	246.59	251.06
β_{xxx}	-33.9	-126.6	-40.6	-192.0	0.0	0.0
β_{zzz}	117.3	23.1	-92.0	-588.4	0.0	0.0
$\gamma_{xxx} \times 10^{-3}$	96.2	119.5	101.8	149.6	72.0	104.0
$\gamma_{zzz} \times 10^{-3}$	79.3	103.7	99.9	141.2	72.0	104.0

31+G(d) basis set, are shown in Table 8.6. The coordinate axes are chosen in such a way that z coincides with the C_3 symmetry axis, and $\beta_{xxx} = 0$. The effect of electron correlation on the hyperpolarizabilities appeared to be significant. The reduction of the magnitude of the hyperpolarizabilities upon encapsulation of Ti into C₂₈ is explained in ref. 49 as a consequence of the localization of the four unpaired electrons due to the bonding between the cage and the Ti atom. This differs from the usual explanation of such effects as a “compression” effect (*e.g.* in ref. 56–59). Comparison with the properties of C₂₈H₄, which are also smaller than those of C₂₈, shows that the explanation advanced in ref. 49 is probably more adequate, as there can be no compression effect in this case.

In addition to the electronic contributions, static vibrational contributions to the electrical properties were also computed in ref. 49, at the so-called double harmonic level. At this level the vibrational contributions are in the Bishop–Kirtman square bracket nomenclature⁶⁰ given by eqn (8.1)–(8.3):

$$\alpha^{\text{DH}} = [\mu^2]^{0,0} \quad (8.1)$$

$$\beta^{\text{DH}} = [\mu\alpha]^{0,0} \quad (8.2)$$

$$\gamma^{\text{DH}} = [\alpha^2]^{0,0} + [\mu\beta]^{0,0} \quad (8.3)$$

These contributions were computed at the restricted Hartree–Fock (RHF) level and at the density functional theory (DFT) level with three different functionals (BLYP, B3LYP, CAM-B3LYP) and the 6-31+G(d) basis set. The values obtained are shown in Table 8.7, where the static electronic contributions are also shown for comparison. For γ^{DH} , only the first term $[\alpha^2]^{0,0}$ was computed. As a prerequisite for the correct computation of vibrational NLO

Table 8.7 Static electronic and double harmonic vibrational contributions to the (hyper)polarizabilities of Ti@C28.

	<i>BLYP</i>	<i>B3LYP</i>	<i>CAM-B3LYP</i>	<i>RHF</i>
α_{xx}^e	272.0	264.4	258.7	258.4
α_{zz}^e	259.9	250.0	241.8	238.6
α_{av}^e	267.9	259.6	253.1	251.8
$[\mu^2]_{0,0}^{0,0}$	21.2	27.1	38.0	58.1
$[\mu^2]_{0,0}^{0,0}$	4.2	3.9	3.8	4.7
$[\mu^2]_{0,0}^{0,0}$	15.5	19.3	26.5	40.3
β_{av}^e	-71.2	-65.7	-66.6	-66.5
β_{yyy}^e	4.3	25.5	61.3	98.6
β_{zzz}^e	7.6	-10.4	-14.1	-34.4
$[\mu\alpha]_{0,0}^{0,0}$	-273.5	-341.4	-448.5	-673.0
$[\mu\alpha]_{0,0}^{0,0}$	6.5	27.4	43.1	69.4
$[\mu\alpha]_{0,0}^{0,0}$	196.2	195.3	275.9	175.4
γ_{av}^e	110	98	85	94
$\gamma_{yyyy}^e \times 10^{-3}$	92	81	70	74
$\gamma_{zzzz}^e \times 10^{-3}$	103	91	79	87
$\gamma_{av}^e \times 10^{-3}$	24	23	22	23
$[\alpha^2]_{yyyy}^{0,0} \times 10^{-3}$	18	16	14	14
$[\alpha^2]_{zzzz}^{0,0} \times 10^{-3}$	21	19	19	19

properties, the computations were performed on geometries optimized at the corresponding level/basis set combination. Thus, the electronic RHF values differ from those in Table 8.6, where the restricted Møller–Plesset second-order perturbation theory RMP2 optimized geometry was used. Additional values were computed in ref. 46 with the smaller 6-31G(d) basis set, and comparison showed that the effect of diffused functions in the basis set is large, especially on the electronic properties (*e.g.* $\gamma_{av}^e = (79-103) \times 10^3$ a.u. with 6-31+G(d), but $(5-7) \times 10^3$ a.u. with 6-31G(d)).

The Table shows that α^{DH} and β^{DH} computed with BLYP and B3LYP functionals are quite similar, but differ substantially from those properties calculated with the long-range corrected CAM-B3LYP potential, suggesting that for these properties the treatment of the xc-potential at long range is important. On the other hand, this seems not to be the case for $[\alpha^2]^{0,0}$. ③

Comparison of electronic and vibrational (DH) contributions shows that for β , the vibrational contribution is much larger than the electronic one, whereas for α and γ the reverse appears to be the case. An analysis of the normal mode contributions to β^{DH} shows that the largest contribution comes from the lowest frequency degenerate pair of e symmetry vibration, which is also associated with a large displacement of the Ti atom with respect to the cage. An energy profile for the normal mode displacement of the mode in question shows that the energy surface for this mode is quite shallow. Therefore, it is reasonable to assume that anharmonic contributions (*i.e.* terms beyond the double harmonic approximation) are important. To illustrate this, the so-

called nuclear relaxation (nr) term for β_{yyy} was calculated at the B3LYP/6-31+G(d) level and found to be 2 000 a.u., several times larger than the DH value. Thus, all the conclusions concerning the relative magnitude of vibrational and electronic contributions to the (hyper)polarizabilities of Ti@C28, based on the DH approximation, should be considered preliminary until higher-level calculations are available. In addition to the nr contribution, which takes only the lowest-order anharmonicities into account, the higher-order c-zpva contribution may also be substantial. A possible treatment of the full range of anharmonicities for the vibrational NLO properties of Ti@C28 using an extension of a recently developed method⁴⁵ is envisaged for future work.

8.5 Analysis of the Binding Energy in Biological Systems

The recognition of different ligands by their receptors is dependent on interactions between them. The type of interactions arising is defined by the chemical structure and the conformations of the molecules. Thus, rational drug design identifies these interactions and opts to enhance them. As is evident from the equation $\Delta G = \Delta H - T\Delta S$ the binding free energy (ΔG) is divided into enthalpic (H) and entropic (S) terms. The structural information of different complexes along with theoretical and experimental free energy estimations offer insight into the relationship between structure and activity. A general observation is that the best drug candidates show enthalpic-driven contributions.⁶¹ For example tipranavir and indinavir – two inhibitors of HIV-1 protease – have very similar entropic contributions ($\sim -14 \text{ kcal mol}^{-1}$), but tipranavir has an enthalpy of $-0.7 \text{ kcal mol}^{-1}$ and indinavir $0.8 \text{ kcal mol}^{-1}$. This difference in the enthalpy term increases the affinity of tipranavir by a factor of 70 to 19 pM.⁶² One of the strongest types of interactions that increases the binding of a drug candidate is hydrogen bonding. The presence of electronegative groups (*e.g.* $-\text{OH}$, $-\text{NH}_2$, $-\text{COOH}$) creates strong H-bond interactions between the ligand and residues of the macromolecule, increasing the enthalpic term in the binding energy.⁶³

Major contributions to the binding energy in a biological system also come from van der Waals and electrostatic interactions. The presence of metal atoms in proteins (*e.g.* metalloproteases) increases the electrostatic interactions between a ligand and the macromolecule.⁶⁴ Wu *et al.*⁶⁵ developed a force field to better monitor the interactions of metals (zinc) with proteins and ligands through quantum mechanics/molecular mechanics (QM/MM) calculations. Shinoda and Tsukube⁶⁶ explored the interactions between cytochrome C and different small molecules, while Villa *et al.*⁶⁷ studied the specificity of the substrate in meprin metalloproteinases and the type of interactions induced by its binding to the enzyme. The COX and LOX proteins are another family of enzymes where electrostatic and hydrophobic interactions are of major importance.⁶⁸ In the LOX family of enzymes the presence of an iron atom at the catalytic site reveals the importance of electrostatic interactions as

shown by a density functional study for the catalytic mechanism of the enzyme by Borowski and Broclawik.⁶⁹

Another important factor to take into account is the environment of the biological system. Hydrophobicity can play an important role in the binding of molecules. Additionally, membrane permeability has great impact in the absorption and activity of a pharmaceutical substance.⁷⁰ Politi *et al.*⁷¹ showed the importance of van der Waals and non-polar interactions in the binding of aliskiren to the active site of renin. Thus, it is vital for researchers to explore options that increase the hydrophobic action of a drug and combine attractive/repulsive (hydrophobic, van der Waals) components.

As mentioned above, hydrogen bonds have a major impact in the binding of a ligand to a biological macromolecule as well as in various enzymatic reactions. Lang *et al.*⁷² explored the impact of hydrogen bonding in the catalysis of oxidation of L-Arg by heme proteins. They specifically focused on residues directly interacting with the heme and the effect mutations have on the catalysis. Yuzlenko and Lazaridis,⁷³ using molecular dynamic techniques, investigated the interactions between ionizable amino acid side chains and lipid bilayers. Their aim was to explore the importance of hydrogen bonding and salt bridges in the stability of large biological systems such as proteins and membranes. Moffett *et al.*⁷⁴ employed *in silico* methods to design optimized p38 α kinase inhibitors. In fact they used fragment-based drug design (FBDD) in order to identify new structures that increase the hydrogen bonding potential with specific residues (*e.g.* Arg70) of the enzyme. NMR spectroscopy has been used by Limbach *et al.*⁷⁵ to investigate the role of the environment in the formation of hydrogen bonds in biological systems. They worked with the enzyme cofactor pyridoxal 5'-phosphate (PLP) in different environments ranging from aqueous solutions to enzyme–substrate systems. Their goal was to understand the effect of the environment in hydrogen bonding better.

Therefore, in drug design interactions play a crucial role. It is important to design ligands so as not only to maximize the binding to the target molecule but also to optimize their interactions with different systems encountered in their path to the target. As shown by Shaw *et al.*,⁷⁶ an extensive study of biological systems can reveal the role of different interactions (*e.g.* van der Waals, hydrophobic, electrostatic) in the system's mode of action. Thus, researchers can have a clearer idea regarding the steps required for the design of a better binding and consequently more effective drug.

Here we shall review the analysis of the binding energy of two fullerene derivatives and C₆₀ with HIV-1 PR. Using the AMBER software package,⁷⁷ molecular dynamics (MD) simulations in explicit solvent were performed in complexes of HIV-1 protease with fullerene derivatives. Fullerene structures are shown in Figure 8.5. The protein–ligand complexes were energy-minimized and subsequently heated to 300 K. The MD simulations were run under constant pressure for 20 ns. Furthermore, the binding energies of the complexes were calculated using the MM-PBSA method.⁷⁸ With this procedure the interactions in each complex are calculated using molecular

(a) (b) (c)

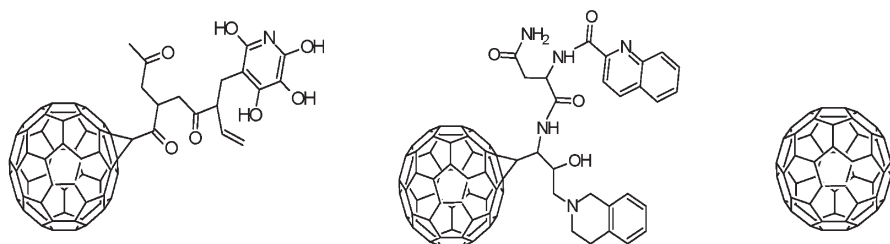


Figure 8.5 Fullerene derivatives studied in complex with HIV-1 PR. (a) Compound 1, (b) compound 2 and (c) fullerene core C_{60} .

mechanics (MM) in the gas phase and the solvation energy is calculated by solving the Poisson–Boltzmann equation. In summary, this method is expressed with the following equations:

$$\Delta G_{\text{bind}} = G_{\text{complex}} - (G_{\text{protein}} + G_{\text{ligand}}) \quad (8.4)$$

$$= \Delta H - T\Delta S \quad (8.5)$$

$$= \Delta E_{\text{MM}} + \Delta G_{\text{solv}} - T\Delta S \quad (8.6)$$

where ΔH is the enthalpy and $T\Delta S$ is the conformational entropy contribution. ΔG_{MM} and ΔG_{solv} are given by:

$$\Delta E_{\text{MM}} = \Delta E_{\text{elec}} + \Delta E_{\text{vdW}} \quad (8.7)$$

$$\Delta G_{\text{solv}} = \Delta G_{\text{PB}} + \Delta G_{\text{NP}} \quad (8.8)$$

ΔG_{PB} is the electrostatic contribution to the solvation free energy. ΔG_{NP} is the non-polar solvation energy, computed by employing the solvent-accessible surface area (SASA), according to the equation:

$$\Delta G_{\text{NP}} = \gamma \text{SASA} + \beta \quad (8.9)$$

As mentioned before, our aim is the investigation of the interactions between the ligand candidates and the target molecules. Therefore the analysis in the

Table 8.8 Contributions to binding energy for three HIV-1 PR complexes.

	ΔE_{elec}	ΔE_{vdW}	ΔG_{NP}	ΔG_{PB}	ΔH	ΔG_{bind}
HIV-1 PR-compound 1	-14.74	-83.90	-26.35	59.92	-65.08	-11.97
HIV-1 PR-compound 2	-20.78	-76.80	-25.14	60.37	-62.35	-12.75
HIV-1 PR-C ₆₀	-5.24	-65.37	-34.25	56.59	-48.27	-1.25

HIV-1 PR complexes focuses on the aspects that offer insights into the type of interactions present. An important feature observed in our simulations is the behavior of the region in the enzyme that encloses the active site. In agreement with experimental studies, we observed that the particular region of the protein traps the ligand into the active site cavity. Further analysis revealed that certain binding-cavity residues form hydrogen bonds with the fullerene derivatives. This behavior can explain the high binding energy observed for the complexes. Unlike the natural substrate of the protease and other inhibitors, the designed fullerene derivatives do not bind directly to the active site of the protein.⁷⁹

As shown in eqn (8.4)–(8.9), with the MM-PBSA technique it is possible to decompose the binding energy to its separate components and identify similarities or differences between the derivatives studied. Table 8.8 summarizes the results from our calculations. The most important aspect of our analysis is the fact that in all three complexes the most significant contribution to the binding energy comes from van der Waals interactions and non-polar contributions to solvation. Comparing the results of the different fullerene derivatives we conclude that the fullerene core is the most important contributor to the van der Waals interactions. The substituents in the fullerenes provide the necessary chemical groups for enhanced interactions with the enzyme, thus increasing the binding energy of the complexes.

8.6 Amino Acid Fullerene Derivatives Bound to HIV-1 PR

The need for new anti-HIV drugs has stimulated a range of research approaches, including the development of drugs that act to inhibit the HIV type I aspartic protease (HIV-1 PR). In this regard, it has been shown that ⁶⁰fullerene and its analogues inhibit HIV-1 PR *via* entrapping of the C₆₀ cage into the hydrophobic binding pocket of the protein, at the interface between the two PR dimers.^{80,81} So far, a large number of potential fullerene derivatives has been reported by several groups for different targets; however, only a few of them have been considered for their HIV-1 PR inhibitory effects.⁸² Despite the almost perfect fit of C₆₀ into the HIV-1 PR binding pocket, both first and second generations of fullerene derivatives have not shown a significant inhibitory effect against HIV-1 PR compared to the standard drugs (*e.g.* amprenavir), which show sub-nanomolar level inhibition. However, their high

stabilities, low cytotoxicities and reduced potential to be processed to the toxic metabolites make them interesting compounds against HIV-1 PR inhibition.⁸³ The synthesis of novel fullerene derivatives and their *in vitro* tests are not easy tasks in the wet-labs and usually require a great deal of effort and time. Therefore, computational techniques can be alternatively used to provide valuable information and may help to derive novel HIV-1 PR inhibitors with improved binding affinities. In this chapter, a successful *in silico* approach for the development of fullerene-based HIV-1 PR inhibitors will be reviewed.^{84–86}

HIV-1 PR belongs to the family of retroviral proteases and is a C_2 symmetric, homodimeric (*i.e.* two identical segments with 99 amino acids each), aspartic protease. The binding site of HIV-1 PR is an open-ended cylindrical hydrophobic cavity of about 10 Å diameter composed of catalytic residues Asp25 and Asp25' (Figure 8.6). Since an X-ray structure of the HIV-1 PR/fullerene analogue complex has not yet been reported, the crystal structure of HIV-1 PR complexed with a haloperidol derivative (pdb: 1AID)⁸⁷ has been used as reference structure for molecular docking and MD simulations.

Molecular docking and MD simulations have been performed with FlexX and GROMACS, respectively. The coordinates of the active-site residues of HIV-1 PR may be different for the case of the HIV-1 PR/fullerene derivative complex compared to the crystallized complex HIV-1 PR/haloperidol. Thus, the correct binding mode of the studied fullerene inhibitors can best be obtained from the MD simulations of HIV-1 PR/fullerene derivative complex.⁸² The best derived docking poses were used as initial geometries for the MD simulations. Since the FlexX docking algorithm uses a rigid target conformation for the protease during the docking simulations, MD studies may assist in generating proper input coordinate for further analyses. In addition, a deeper understanding of the mechanistic events associated with HIV-1 PR binding can be also achieved by analyzing the MD trajectories.⁸²

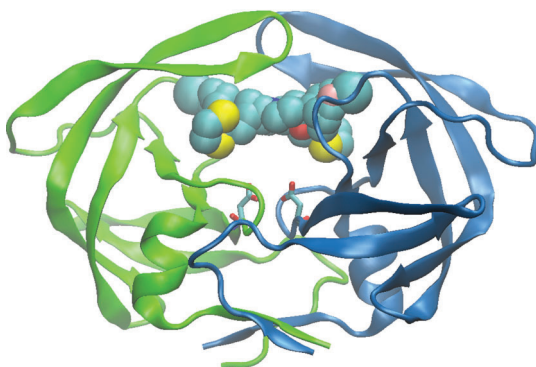


Figure 8.6 Structural representation of HIV-1 PR: C_2 symmetric, homodimeric (*i.e.* two identical segments with 99 amino acids each), aspartic protease. Figure shows haloperidol-bound HIV-1 PR.

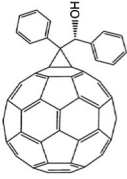
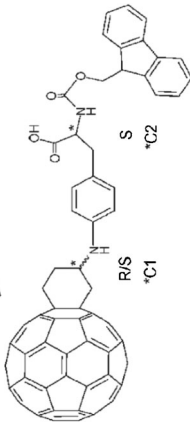
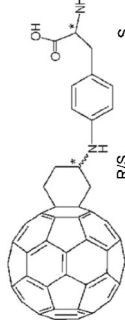
Thus, together with the fullerene-bound complex, a control (HIV-1 PR without fullerene inhibitor) MD simulation was also performed. Consistent structural differences have been observed between the fullerene-free and fullerene-bound systems of the HIV-1 PR. In the fullerene-bound forms, the flaps are pulled in toward the dual Asp25 catalytic site (closed form), while the structure for the free HIV-1 PR flaps shifted away from the catalytic site (semi-open form).⁸²

The coordinate file for the fullerene-bound HIV-1 PR produced from the MD simulations has been used and tested for the docking scores. The predicted pIC_{50} values of the fullerene derivatives have been compared to the actual pIC_{50} values and a high correlation between them has been found. Thus, a database that includes more than 100 fullerenes has been constructed by searching the ⁶⁰fullerene derivatives in the literature.⁸⁶ These fullerene analogues have been synthesized in the past decade and most of them were designed for other biomedical applications. Since MD simulations assisted in obtaining the correct enzyme input coordinates for docking the fullerene analogues, compounds in the database have been docked to the target and their binding scores and binding interactions were compared. One group of compounds showed particular promise: fullerene-based peptidic derivatives and their structural analogues.^{86,88,89} Their high affinities are connected with the ability of pendant groups to form H-bonds and electrostatic interactions with the catalytic active site of the enzyme as well as van der Waals interactions between the fullerene cage and the non-polar surface of active site amino acid residues.⁸⁶ The structures that showed better binding scores than the currently reported most potent fullerene-based HIV-1 PR inhibitor (compound **1**, Table 8.9) were collected and subjected to biological tests. These *in vitro* analyses proved the computational predictions: The bucky amino acid (compound **3S**, Table 8.9) showed a similar binding affinity ($K_i = 120$ nM) with to compound **1** ($K_i = 103$ nM). Furthermore, the 9-fluorenylmethoxycarbonyl-protected bucky amino acid (compound **2S**, Table 8.9) showed about 3-fold better activity ($K_i = 36$ nM) than the most active currently available fullerene derivative **1**.^{86,89}

This is considered to be an important finding because a new anti-HIV fullerene derivative is proposed, which is approximately 3-fold more active than those which have been reported and it is expected to stimulate further research for even more effective anti-HIV drugs. Moreover, it can be useful for directing future three-dimensional quantitative structure–activity relationships (3D-QSAR) studies. Obviously, when the number of compounds in the data set used for 3D-QSAR studies increases, the stability of the constructed QSAR model and the output from the model is expected to be increased. Therefore, each new measurement of fullerene derivatives adds valuable data for 3D-QSAR studies which help to understand the steric and electrostatic requirements of HIV-1 PR inhibition. Thus, these inhibition data of novel fullerene derivatives will assist in the diverse range of binding affinity values and will be very useful also for future 3D-QSAR studies.

4

Table 8.9 Comparison of experimental and computational binding energies and binding affinities of fullerene amino acid derivatives at HIV-1 PR. The binding affinity of compound **1** at HIV-1 PR was reported in ref. 90 and the binding affinities of **2S** and **3S** were reported in a recent publication.⁸⁶

Compound no.	Structure	Experimental binding affinities, $K_i/\mu\text{M}$	Experimental binding energies/ kJ mol^{-1}	Computational (docking) binding energies/ kJ mol^{-1}
1		103	-40.13	-36.66
2S		36	-42.75	-43.54 (*C1, S) -39.40 (*C1, R)
3S		120	-39.75	-37.60 (*C1, S) -36.56 (*C1, R)

8.7 MMK16 into COX-2/LOX-5 Enzymes

Enzymes cyclooxygenase-2 (COX-2)⁹⁰ and lipoxygenase-5 (LOX-5)⁹¹ have been implicated in inflammation responses and in the progression of neoplasia.^{90,92–94} Toward the development of potent anti-inflammatory compounds, MMK pyrrolidinone-based analogues have been synthesized to inhibit both enzymes.^{95,96} 4-[(2S)-2-(1*H*-imidazol-1-ylmethyl)-5-oxotetrahydro-1*H*-pyrrol-1-yl]methylbenzenecarboxylic acid (MMK16) is a promising candidate inhibitor since it possesses pyrrolidinone and carboxylate groups, which are both associated with anti-inflammatory action.^{97,98}

Molecular dynamics (MD) and molecular docking techniques provided useful information regarding principal interactions between MMK16 and COX-2/LOX-5 as well as a dynamic description of the systems by monitoring conformational changes induced upon binding.⁹⁸ Aspirin and caffeic acid are known inhibitors of COX-2 and LOX-5, respectively. Thus, comparative docking calculations for MMK16 into COX-2 and for aspirin into COX-2 suggested that MMK16 is a more potent inhibitor of the enzyme than aspirin mainly due to the orientation of MMK16 in the binding cavity and the stabilization of its structure *via* electrostatic interactions. Similarly, electrostatic interactions between the catalytic Fe(III) in LOX-5 and the imidazole ring of MMK16 favor binding of MMK16 (compared to caffeic acid) into LOX-5. Hydrogen bonding (HB) and van der Waals interactions further stabilize MMK16 inside COX-2/LOX-5.

Additionally, a 12 ns all-atom MD simulation in an implicit solvent environment⁹⁹ at 300 K for the MMK16–COX-2 system resulted in a stable structure for the enzyme, after an initial conformational change, which was induced mainly by the increased flexibility of residues belonging to the membrane-binding domain and active-site region (Figure 8.7a). This implied that the initial, docked structure of MMK16 may be unstable and rather equilibrates toward different conformations. Indeed, HB analysis showed the rearrangement of interactions during the course of the simulation: the initial HB interaction between the imidazole ring of MMK16 and active-site residue Arg120 was replaced by another interaction between the pyrrolidinone oxygen atom of MMK16 and Arg120. This HB rearrangement resulted in a displacement of MMK16 to a new position that favors enhanced interactions with the binding cavity. Although the active site (His90, Arg120, Gln192, Tyr355, Arg513, Val523, Glu524) appeared overall stable, it underwent a substantial structural change to account for the new arrangement of MMK16. Additional interactions such as MMK16–Ser530 and MMK16–Asp362 stabilized further MMK16 into COX-2 (Figure 8.7b).

A representation of MMK16 into the binding cavity of LOX-5 is given in Figure 8.7c. A noticeable conformational change was also observed for LOX-5 upon beginning the 12 ns MD simulation of the MMK16–LOX-5 complex. However, structural changes on this enzyme were considered irrelevant to the active site since the latter appeared practically stable throughout the simulation and it did not participate in any HB interactions with MMK16.

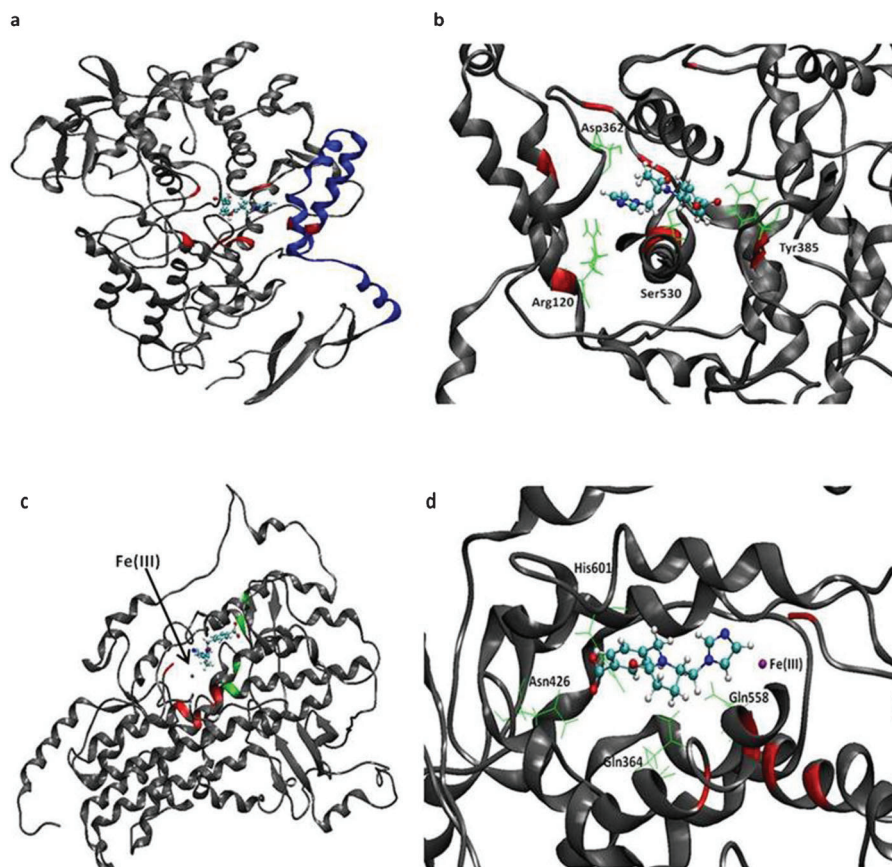


Figure 8.7 (a) Schematic representation of MMK16 into COX-2. Active-site residues (His90, Arg120/513, Gln192, Tyr355, Val523, Glu524, in red) form a tunnel through which inhibitors bind to the catalytic cavity of the enzyme. The flexible membrane-binding domain (residues 73–123, in blue) induces structural changes to COX-2. (b) Close-up view of MMK16 into COX-2 binding cavity. Residues forming hydrogen bonds with MMK16 are shown in green. (c) Schematic representation of MMK16 into LOX-5. Residues involved in hydrogen bonds with MMK16 (Gln364/558, Asn426, His601, in green) do not belong to the active-site region (His368/373/551, Asn555, Ile674, in red). Catalytic Fe(III) is in constant interaction with MMK16. (d) Close-up view of MMK16 into LOX-5 binding cavity. Residues forming hydrogen bonds with MMK16 are shown in green and Fe(III) in purple.

Additionally, atomic fluctuation calculations for active-site residues (His368, His373, His551, Asn555, Ile674) yielded values well below 1 Å, thus indicating the very low mobility of this region. In accordance with the docking results, the distance between the imidazole ring and the catalytic Fe(III) in the active site remained very stable during the simulation around the average 2.15 Å. HB analysis revealed the main reason for the structural change induced to LOX-5

during the beginning of the simulation: the initially unstable MMK16–His433 interaction has been gradually replaced by a strong HB network involving interactions between MMK16 and non-active-site residues Gln364, Asn426, Gln558 and His601 (Figure 8.7d).

Finally, the ability of MMK16 to exclude water from the the enzymes' binding cavities was explored to reveal that the solvent-accessible surface area (SASA) of the compound inside COX-2 appeared almost 2-fold greater than inside LOX-5. Since it is anticipated that a strong hydrophobic environment may act favorably toward binding in COX/LOX systems, the exposure of MMK16 to the solvent may play a crucial role.

8.8 Aliskiren in Solution and Bound to Renin

Renin inhibition is of paramount importance toward effective therapeutic strategies against hypertension.^{100,101} Renin is a 340-amino acid, highly selective aspartic protease, which cleaves angiotensinogen to produce peptide angiotensin I.¹⁰² An increase in blood pressure occurs when angiotensin I is converted to angiotensin II by the angiotensin-converting enzyme (ACE). The active site of renin is a deep cavity to the bottom of which a pair of catalytic triads (Asp32/215, Thr33/216, Gly34/217) lies.^{102,104} In 2007, aliskiren was approved by the US Food and Drug Administration (FDA) as the first oral renin inhibitor for the treatment of hypertension.^{105–107} It possesses four chiral centers and prevents the conversion of angiotensinogen to angiotensin I upon direct binding to the catalytic cavity of renin. A highly potent inhibitor for human renin, aliskiren has $IC_{50} = 0.6$ nM and biological half life ≈ 24 h.¹⁰⁸

In a recent study, Politi *et al.* investigated the conformational properties of aliskiren in dimethylsulfoxide (DMSO) using MD calculations and NMR spectroscopy.⁷¹ The X-ray crystal structure of aliskiren was solvated in DMSO and heated at 300 K before being subjected to a lengthy MD simulation for 200 ns. The trajectory obtained after the simulation was next clustered to group aliskiren structures based on conformational similarities as defined by a 2.5 Å cutoff among all conformations. In agreement with the NMR results, clustering analysis revealed that aliskiren appeared flexible and adopts two main conformations in DMSO solution. The first representative structure was dominant during the simulation (73% of time present) and suggested an extended conformation for aliskiren, while the second representative structure appeared for 27% of the simulation and denoted a “bent” structure. Of major significance was the observation that the extended conformation of aliskiren bore a striking resemblance to the crystal structure of the drug when bound to renin (Figure 8.8a). Therefore the use of the crystal structure as the initial structure to investigate the dynamic properties and binding modes of aliskiren in renin could be well rationalized.

Thus, the same authors were the first to perform MD simulations and MM–PBSA free energy calculations for the aliskiren–renin complex to explore binding patterns, principal interactions and conformational changes associated

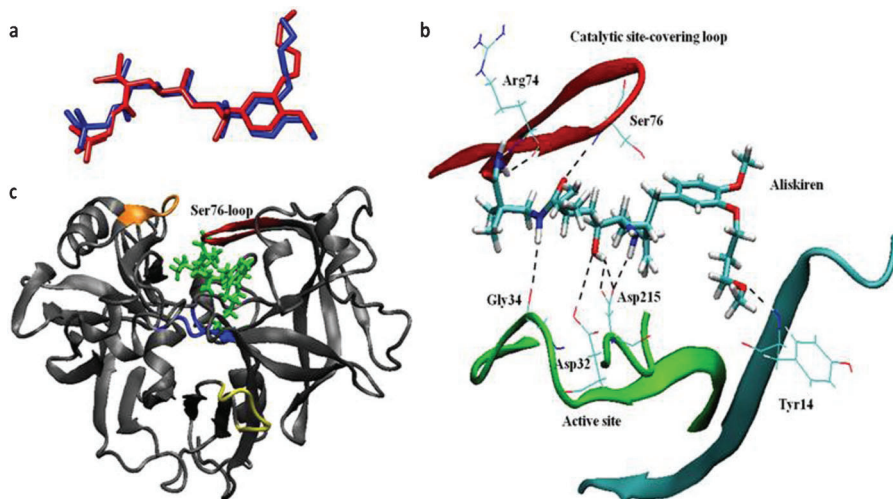


Figure 8.8 (a) The representative structure of aliskiren in DMSO (obtained after clustering calculations, red) resembles the crystal structure of aliskiren (blue). (b) Principal hydrogen bonds between aliskiren and renin: eight interactions involving active-site and Ser76-loop residues stabilize the drug inside the protease. (c) The very mobile Ser76 loop in the *apo* form of renin is stabilized in a closed conformation upon aliskiren entrapping into the binding cavity. Aliskiren (green) lies on top of the active site (blue) in an extended conformation.

with aliskiren binding to renin.⁷¹ A 15 ns MD simulation at 300 K and in explicit water was initiated from the X-ray crystal structure of aliskiren–renin to observe that the complex presented a high degree of stability, further suggesting that the simulated system equilibrates toward conformations that resemble the crystal structure. HB analysis attributed the increased stability of the complex to several HB interactions between aliskiren and active-site residues of renin. The major HB interactions between aliskiren and renin are presented in Figure 8.8b. In particular, Asp32/215 and Gly34 at the active site are involved in stabilizing the drug inside the cavity of renin, while residues such as Arg74, Ser76 and Tyr14 also participate in HB interactions with aliskiren. 6

Although the structure of the complex remained stable during the simulation, a striking feature was observed when the flexibility of the *apo* (ligand-free) form of renin was considered. Amino acid residues in the vicinity of the “tip” residue Ser76 (Arg74–Tyr75–Ser76–Thr77–Gly78) form a loop that belongs to the outer region of the protease, lying on top of the active site. This loop appeared increasingly flexible in the *apo* renin, with “open” and “closed” conformations being in dynamic equilibrium. This suggested that ligand access to the cavity may depend on the sufficient opening of this loop. This was a direct implication of this region as being a modulator for substrate entrance to the binding cavity of renin. Interestingly, upon aliskiren binding to

renin, the loop stabilized permanently *via* two HB among Arg74, Ser76 and aliskiren. Ser76 remained attached to aliskiren in a closed conformation that entrapped the drug inside renin to yield a compact structure stabilized by strong interactions involving active-site residues, the loop and aliskiren (Figure 8.8b and c).

Finally, MM-PBSA free-energy calculations were applied to estimate the binding energy in the aliskiren–renin complex to be $-12.0 \text{ kcal mol}^{-1}$, in agreement with the experimental value ($-12.6 \text{ kcal mol}^{-1}$).¹⁰⁹ Further energy decomposition revealed that the formation of the complex is mainly driven by the non-polar contribution to solvation ($-28.1 \text{ kcal mol}^{-1}$) and by van der Waals ($-35.7 \text{ kcal mol}^{-1}$) interactions. As this trend has been already verified in other protein complexes by independent studies, it could be used as an effective tool for compound optimization in drug design.^{110,111}

8.9 Drug–Biosurface Interactions

Recent reviews point out the significance of drug–membrane interactions.^{112–115} This is because of two major reasons. First, some classes of drug molecules act directly at the lipid bilayer core, perturbing the lipid component or triggering the modulation of the proteins, and some others still have to interact with the membranes in order to reach their interior site of action. It is for these reasons that intense studies have been applied in recent decades to study the efficiency of drugs when interacting with the membranes and correlate it with their pharmacological effects. At the moment such a correlation is not straightforward and to analyze the fingerprint of the drug in the membranes is tedious work and implies the application of many biophysical methodologies. Thanks to advances in the capabilities of analytical instrumentation and methodologies developed that aided in the acquiring of detailed information on drug–membrane interactions,^{116–146} this is becoming more straightforward. 7

Membrane bilayers are complex entities composed of different proteins and lipids. Both components are very important for a drug to exert its biological effect. In our studies we have focused on the drug action at the lipid component of the membranes. Here we will give an example from our recent work to illustrate the importance of the drug–membrane interactions. It has been proposed that antihypertensive drugs, and more particularly the AT₁ antagonists which act through blocking vasoconstrictive hormone angiotensin II, are first embedded into the lipid bilayers and then through lateral diffusion reach the active site of their receptor. The molecular basis of AT₁ antagonist action is shown in Figure 8.9.^{147–154}

It is evident that lipid bilayers play an important role in AT₁ antagonism. For this reason we found it very interesting to study the membrane–AT₁ interactions. Thus, it appears very important to relate the fingerprint of an AT₁ antagonist and its pharmacological action (Figure 8.10). *This would lead to the synthesis of drugs possessing more specific and better pharmacokinetic properties.*

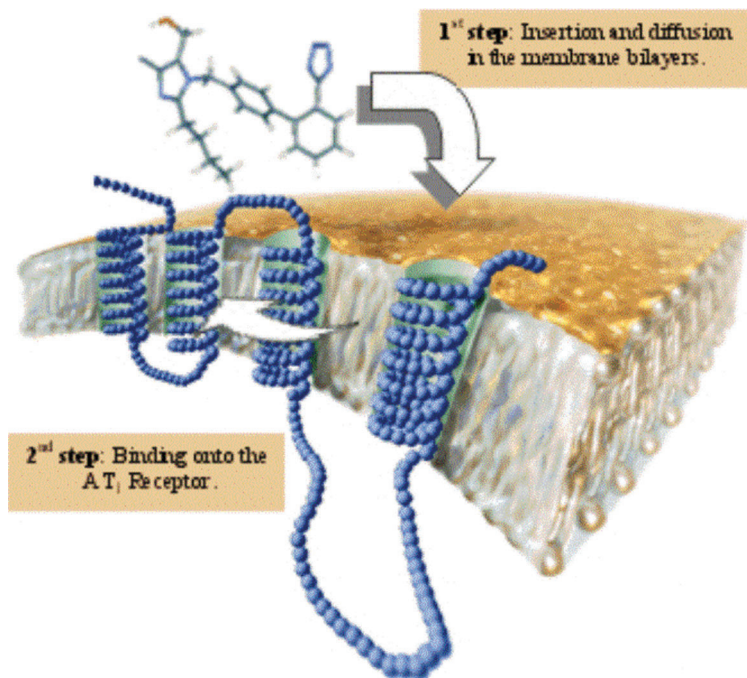


Figure 8.9 The mechanism of action for the prototype of AT₁ antagonists, losartan. 8

First, we defined the properties of the drugs in the lipid bilayers that determine their fingerprints and then we attempted to quantify them using various physical and chemical methodologies. Such properties are: (a) topography (localization); (b) perturbation as it is depicted by *gauche*–*trans* isomerization and chain mobility.

To show the importance of drug–membrane interactions we provide an example of a comparative study between the two drugs losartan and candesartan cv (see Figure 8.11 and ref. 151).

Losartan (Cozaar) is the first commercially developed competitive/surmountable antihypertensive AT₁ antagonist of the sartans class. Candesartan (CV-11974) is a non-competitive/insurmountable antagonist

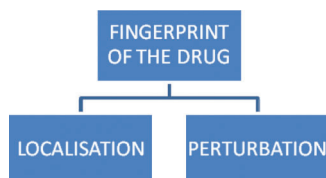


Figure 8.10 The fingerprint of the drug is determined by its orientation, localization and a general perturbation term which includes its thermal, dynamic and other effects that can be quantified.

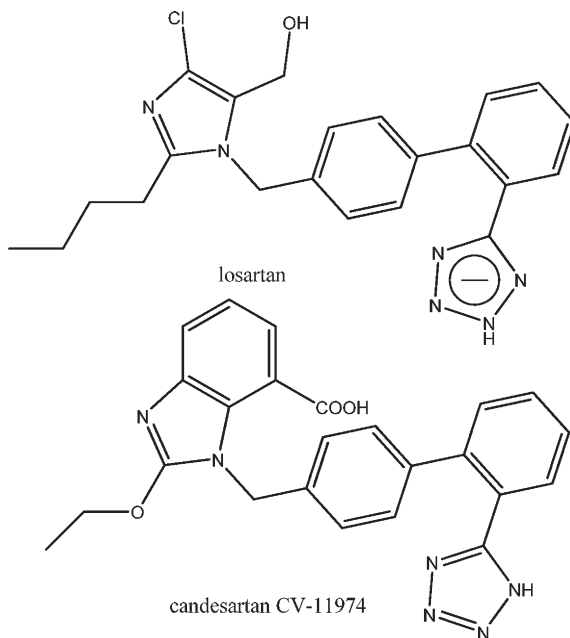


Figure 8.11 Chemical structures of losartan and candesartan CV-11974.

and is the active metabolite of candesartan cilexetil (Atacand), which belongs to the sartan class. Compared to losartan it exerts a longer duration of action and shows the highest receptor affinity among the AT₁ sartan antagonists.^{155,156}

At the given experimental conditions (pH ~ 7), both the acidic tetrazole and carboxylate groups of candesartan are mostly deprotonized ($pK_a \sim 6$ for the tetrazole ring and $pK_a \sim 3-4$ for the carboxylic acid). Losartan is in a potassium salt form and bears only the acidic group of tetrazole with a negative charge. Dipalmitoylphosphatidylcholine (DPPC) is a neutral zwitterionic molecule at physiological pH, bearing the positively charged headgroup choline and the negatively charged phosphate moiety. It is anticipated that the two agents would exhibit different electrostatic interactions with the bilayer interface due to the difference in their negative charges, implying a differentiated affinity to the membrane surface as well as a different immersion of the drugs in the model membranes.

The interactions of the two molecules were studied through the application of differential scanning calorimetry (DSC), Raman, and solid-state ³¹P NMR spectroscopies. A ³¹P CP NMR broadline fitting methodology in combination with *ab initio* computations was implemented and, in conjunction with DSC and Raman results, provided valuable information regarding the perturbation, localization, orientation, and dynamic properties of the drugs in membrane models.

In particular, losartan is localized at the interface which covers the polar region and upper segment of the lipophilic region to maximize its amphipathic interactions. Such a localization of the drug could induce a local curvature and enlarge the space between the adjacent alkyl chains. This could allow the tails of the alkyl chains of the next layer to entangle, introducing tail interdigitation. On the other hand, candesartan at low concentrations affects only the headgroup, probably spanning between the water interface and headgroup region. This may be attributed to attractive electrostatic interactions between the two anions of candesartan and the positively charged nitrogen atom of the choline group, and repulsive interactions with the phosphate group, thus leading to its higher affinity for aggregation with the water interface as it adopts a more accessible area to the hydrophilic environment. At higher concentrations, candesartan strengthens the polar interactions and also affects the packing of the alkyl chains, probably due to partial penetration into the hydrocarbon region.

Both sartan molecules decrease the mobilization of the phospholipid alkyl chains. Losartan exerts stronger interactions in comparison to candesartan, as depicted by the more prominent thermal, structural, and dipolar ^1H - ^{31}P changes that are caused in the lipid bilayers. At higher concentrations, candesartan strengthens the polar interactions and induces increased order at the bilayer surface. At the highest concentration used (20 mol%), only losartan induces the formation of microdomains attributed to the flexibility of its alkyl chain. The comparative perturbing effects and interface activity of the molecules are shown in Tables 8.10 and 8.11.

The above observed variations in membrane interactions might relate to the differentiated pharmacological profile of the two studied AT_1 antagonists and plausibly in part explain the more potent biological profile of candesartan. In addition, the obtained results suggest a relationship between the diffusion efficacy and the pharmacological potency of the studied sartan agents. Thus, losartan's tendency to form domains in the lipid bilayers could presumably retard its diffusion toward the active site of the AT_1 receptor. Moreover, the

Table 8.10 Comparison of interface activity of candesartan CV-11974 and losartan in phosphatidylcholine bilayers.

Methodology	Effect	Candesartan	
		CV-11974	Losartan
Differential scanning calorimetry	Inhibition of pre-transition	No inhibition	Inhibition
Raman spectroscopy	Shift of 714 cm^{-1} peak attributed to C-N stretch vibration	Shift to higher values	Shift to higher values
^{31}P NMR spectroscopy	Lowers σ_{iso} values	Lowers σ_{iso} values	More significant lowering of the σ_{iso} values

Table 8.11 Comparison of the perturbing effect of candesartan CV-11974 and losartan in phosphatidylcholine bilayers.

<i>Methodology</i>	<i>Effect</i>	<i>Candesartan CV-11974</i>	<i>Losartan</i>
Differential scanning calorimetry	Abolishing the pre-transition lowers the value of the main phase transition temperature and causes broadening	No abolition, small effect	Abolition, stronger lowering of the main phase transition and broadening
Raman spectroscopy	$I_{2935/2880}$ ratio	Lowering	More drastic lowering

diffusion may be retarded by its stronger binding to the headgroup region as well as the induction of the interdigitation effect. On the other hand, candesartan at higher concentration is not inhibited by such effects toward its diffusion trip at the AT₁ receptor. Its membrane perturbation effects are milder and, in contrast to losartan, its incorporation does not induce interdigitation to the lipid matrix.

Acknowledgments

H. Tzoupis acknowledges the following: This research has been co-financed by the European Union (European Social Fund – ESF) and Greek national funds through the Operational Program “Education and Lifelong Learning” of the National Strategic Reference Framework (NSRF) – Research Funding Program: Heracleitus II. Investing in knowledge society through the European Social Fund. G. Leonis acknowledges the funding provided by the European Commission for the FP7-REGPOT-2009-1 Project ‘ARCADE’ (Grant Agreement No. 245866). M. G. Papadopoulos acknowledges the High-Performance Computing Infrastructure for South East Europe’s Research Communities (HP-SEE), a project co-funded by the European Committee (under Contract No. 261499) through the Seventh Framework Programme. Also we acknowledge the CINECA award under the ISCRA initiative, for the availability of high-performance computing resources and support.

References

1. H. W. Kroto, J. R. Heath, S. C. O’Brien, R. F. Curl and R. E. Smalley, *Nature*, 1985, **318**, 162.
2. P. Avouris, *Acc. Chem. Res.*, 2002, **35** 1026.
3. P. Delaney and J. C. Greer, *Appl. Phys. Lett.*, 2004, **84**, 431.
4. A. Gromov, N. Krawez, A. Lassesson, D. I. Ostrovskii and E.E.B. Campbell, *Curr. Appl. Phys.*, 2002, **2**, 51.
5. H. Shinohara, *Rep. Prog. Phys.*, 2002, **63**, 843.

6. L. Dunsch and S. Yang, *Electrochem. Soc. Interface*, 2006, **15**, 34.
7. Y. Chai, T. Guo, C. Jin, R. E. Haufler, L. P. F. Chibante, J. Fure, L. Wang, J. M. Alford and R. E. Smalley, *J. Phys. Chem.*, 1991, **95**, 7564.
8. R. Beyers, C.-H. Kiang, R. D. Johnson, J. R. Salem, M. S. de Vries, C. S. Yannoni, D. S. Bethune, H. C. Dorn, P. Burbank, K. Harich and S. Stevenson, *Nature*, 1994, **370**, 196.
9. D. S. Bethune, R. D. Johnson, J. R. Salem, M. S. de Vries and C. S. Yannoni, *Nature*, 1993, **366**, 123.
10. D. E. Manolopoulos and P. W. Fowler, *Chem. Phys. Lett.*, 1991, **187**, 12.
11. P. W. Fowler and D. E. Manolopoulos, *An Atlas of Fullerenes*, Oxford University Press, Oxford, 1995.
12. K. Kobayashi and S. Nagase, *Chem. Phys. Lett.*, 1996, **262**, 227.
13. S. Guha and K. Nakamoto, *Coord. Chem. Rev.*, 2005, **249**, 1111.
14. I. Infante, L. Gagliardi and G. E. Scuseria, *J. Am. Chem. Soc.*, 2008, **130**, 7459.
15. A. Rehaman, L. Gagliardi and P. Pyykkö, *Int. J. Quantum Chem.*, 2007, **107**, 1162.
16. Z. Slanina, Z. Chen, P.v.R. Schleyer, F. Uhlik, X. Lu and S. Nagase, *J. Phys. Chem. A*, 2006, **110**, 2231.
17. L. Dunsch, A. Bartl, P. Georgi and P. Kuran, *Synth. Met.*, 2001, **121**, 1113.
18. K. Ohno, Y. Maruyama, K. Esfarjani, Y. Kawazoe, N. Sato, R. Hatakeyama, T. Hirata and M. Niwano, *Phys. Rev. Lett.*, 1996, **76**, 3590. 9
19. M. S. Syamala, R. J. Gross and M. Saunders, *J. Am. Chem. Soc.*, 2002, **124**, 6216.
20. T. Cai, L. Xu, H. W. Gibson, H. C. Dorn, C. J. Chancellor, M. M. Olmstead and A. L. Balch, *J. Am. Chem. Soc.*, 2007, **129**, 10795.
21. C. R. Wang, T. Kai, T. Tomiyama, T. Yoshida, Y. Kobayashi, E. Nishibori, M. Takata, M. Sakata and H. Shinohara, *Nature*, 2000, **408**, 426.
22. S. Stevenson, P. W. Fowler, T. Heine, J. C. Duchamp, G. Rice, T. Glass, K. Harich, E. Hajdu, R. Bible and H. C. Dorn, *Nature*, 2000, **408**, 427.
23. Z. Q. Shi, X. Wu, C. R. Wang, X. Lu and H. Shinohara, *Angew. Chem., Int. Ed.*, 2006, **45**, 2107.
24. S. Yang, A. A. Popov and L. Dunsch, *Angew. Chem., Int. Ed.*, 2007, **46**, 1256.
25. H. Kato, A. Taninaka, T. Sugai and H. Shinohara, *J. Am. Chem. Soc.*, 2003, **125**, 7782.
26. T. Wakahara, H. Nikawa, T. Kikuchi, T. Nakahodo, G. M. A. Rahman, T. Tsuchiya, Y. Maeda, T. Akasaka, K. Yoza, E. Horn, K. Yamamoto, N. Mizorogi, Z. Slanina and S. Nagase, *J. Am. Chem. Soc.*, 2006, **128**, 14228.
27. Z. Slanina, F. Uhlik, S.-L. Lee, L. Adamowicz and S. Nagase, *Int. J. Quantum Chem.*, 2007, **107**, 2494.
28. S. Yang, A. A. Popov and L. Dunsch, *J. Phys. Chem. B*, 2007, **111**, 13659.

29. C. M. Beavers, T. Zuo, J. C. Duchamp, K. Harich, H. C. Dorn, M. Olmstead and A. L. Balch, *J. Am. Chem. Soc.*, 2006, **128**, 11352.
30. M. M. Olmstead, H. M. Lee, J. C. Duchamp, S. Stevenson, D. Marciu, H. C. Dorn and A. L. Balch, *Angew. Chem., Int. Ed.*, 2003, **42**, 900.
31. K. Kobayashi and S. Nagase, in *Endofullerenes: A New Family of Carbon Clusters*, ed. T. Akasaka and S. Nagase, Kluwer Academic Publishers, Dordrecht, The Netherlands, 2002, p. 99.
32. T. S. M. Wan, H. W. Zhang, T. Nakane, Z. D. Xu, M. Inakuma, H. Shinohara, K. Kobayashi and S. Nagase, *J. Am. Chem. Soc.*, 1998, **120**, 6806.
33. Y.-H. Cui, W. Q. Tian, J.-K. Feng and D.-L. Chen, *J. Comput. Chem.*, 2008, **29**, 2623.
34. R. Tellgmann, N. Krawez, S.-H. Lin, I. V. Hertel and E. E. B. Campbell, *Nature*, 1996, **382**, 407.
35. D. B. Whitehouse and A. D. Buckingham, *Chem. Phys. Lett.*, 1993, **207**, 332.
36. M. R. Pederson, T. Baruah, P. B. Allen and C. Schmidt, *J. Chem. Theory Comput.*, 2005, **1**, 590.
37. E. E. B. Campbell, M. Fanti, I. V. Hertel, R. Mitzmer and F. Zerbetto, *Chem. Phys. Lett.*, 1998, **288**, 131.
38. E. E. B. Campbell, S. Couris, M. Fanti, E. Koudoumas, N. Krawez and F. Zerbetto, *Adv. Mater.*, 1999, **11**, 405.
39. M. Yaghoobi, R. Rafie and A. Koohi, *J. Mol. Struct.: THEOCHEM*, 2009, **905**, 48.
40. M. Yaghoobi and A. Koohi, *Mol. Phys.*, 2010, **108**, 119.
41. H. Reis, O. Loboda, A. Avramopoulos, M. G. Papadopoulos, B. Kirtman, J. M. Luis and R. Zalesny, *J. Comput. Chem.*, 2011, **32**, 908.
42. M. Zhang, L. B. Harding, S. K. Gray and S. A. Rice, *J. Phys. Chem. A*, 2008, **112**, 5478.
43. J. Hernandez-Rojas, J. Breton and J. M. Gomez-Lllorente, *Chem. Phys. Lett.*, 1995, **235**, 160.
44. P. W. Fowler and P. A. Madden, *Phys. Rev. B*, 1984, **30**, 6131.
45. J. M. Luis, H. Reis, M. G. Papadopoulos and B. Kirtman, *J. Chem. Phys.*, 2009, **131**, 34116.
46. <http://www.theochem.uni-stuttgart.de/pseudopotentials/clickpse.en.html>.
47. J. M. Luis, M. Duran, B. Champagne and B. Kirtman, *J. Chem. Phys.*, 2000, **113**, 5203.
48. O. Loboda, R. Zalesny, A. Avramopoulos, J. M. Luis, B. Kirtman, N. Tagmatarchis, H. Reis and M. G. Papadopoulos, *J. Phys. Chem. A*, 2009, **113**, 1159.
49. B. Skwara, R. W. Gora, R. Zalesny, P. Lipkowski, W. Bartkowiak, H. Reis, M. G. Papadopoulos, J. M. Luis and B. Kirtman, *J. Phys. Chem. A*, 2011, **115**, 10370.
50. T. Guo, R. E. Smalley and G. E. Scuseria, *J. Chem. Phys.*, 1993, **99**, 352.

51. B. L. Dunlap, O. D. Haberlen and N. J. Rosch, *J. Phys. Chem.*, 1992, **96**, 9095.
52. R. Bauernschmitt, R. Ahlrichs, F. Hennerich and M. Kappes, *J. Am. Chem. Soc.*, 1998, **120**, 5052.
53. C. A. Jimenez-Hoyos, B. G. Janesko and G. E. Scuseria, *Phys. Chem. Chem. Phys.*, 2008, **10**, 6621.
54. M. D. Halls and H. B. Schlegel, *J. Chem. Phys.*, 1998, **109**, 10587.
55. M. D. Halls and H. B. Schlegel, *J. Chem. Phys.*, 1999, **111**, 8819.
56. M. G. Papadopoulos and A. J. Sadlej, *Chem. Phys. Lett.*, 1998, **288**, 377.
57. P. W. Fowler and P. A. Madden, *Phys. Rev. B*, 1984, **29**, 1035.
58. P. W. Fowler, *J. Phys. Chem.*, 1985, **89**, 2581.
59. A. Kaczmarek and W. Bartkowiak, *Phys. Chem. Chem. Phys.*, 2009, **11**, 2885.
60. B. Kirtman, B. Champagne and J.M. Luis, *J. Comput. Chem.*, 2000, **16**, 1572.
61. C. Bissantz, B. Kuhn and M. Stahl, *J. Med. Chem.*, 2010, **53**, 5061.
62. E. Freire, *Drug Discovery Today*, 2008, **13**, 869.
63. C. A. Lipinski, F. Lombardo, B. W. Dominy and P. J. Feeney, *Adv. Drug Delivery Rev.*, 1997, **23**, 3.
64. P. Caccina, O. Rossettoa, M. Rigoni, E. Johnson, G. Schiavoc and C. Montecucco, *FEBS Lett.*, 2003, **542**, 132.
65. R. Wu, Z. Lu, Z. Cao and Y. Zhang, *J. Chem. Theory Comput.*, 2011, **7**, 433
66. S. Shinoda and H. Tzukube, *Chem. Sci.*, 2011, **2**, 2301.
67. J. P. Villa, G. P. Bertenshaw and J. S. Bond, *J. Biol. Chem.*, 2003, **278**(43), 42545.
68. E. Pontiki, D. Hadjipavlou-Litina, K. Litinas, O. Nicolotti and A. Carotti, *Eur. J. Med. Chem.*, 2011, **46**(1), 191.
69. T. Borowski and E. Broclawik, *J. Phys. Chem. B*, 2003, **107**, 4639.
70. E. H. Mojumbar and A. P. Lyubartsev, *Biophys. Chem.*, 2010, **153**, 27.
71. A. Politi, G. Leonis, H. Tzoupis, D. Ntountaniotis, M. G. Papadopoulos, S. G. Grdadolnik and T. Mavromoustakos, *Mol. Inf.*, 2011, **30**, 973.
72. J. Lang, J. Santolini and M. Couture, *Biochemistry*, 2011, **50**, 10069.
73. O. Yuzlenko and T. Lazaridis, *J. Phys. Chem. B*, 2011, **115**, 13674.
74. K. Moffett, Z. Konteatis, D. Nguyen, R. Shetty, J. Ludington, T. Fujimoto, K. J. Lee, X. Chai, H. Namboodiri, M. Karpusas, B. Dorsey, F. Guarnieri, M. Bukhtiyarova, E. Springman and E. Michelotti, *Bioorg. Med. Chem. Lett.*, 2011, **21**, 7155.
75. H. H. Limbach, M. Chan-Huot, S. Sharif, P. M. Tolstoy, I. G. Shenderovich, G. S. Denisov and M. D. Toney, *Biochim. Biophys. Acta*, 2011, **1814**, 1426.
76. B. F. Shaw, G. F. Schneider, H. Arthanari, M. Narovlyansky, D. Moustakas, A. Durazo, G. Wagner and G. M. Whitesides, *J. Am. Chem. Soc.*, 2011, **133**, 17681.

77. D. A. Case, T. A. Darden, T. E. Cheatham III, C. L. Simmerling, J. Wang, R. E. Duke, R. Luo, R. C. Walker, W. Zhang, K. M. Merz, B. P. Roberts, B. Wang, S. Hayik, A. Roitberg, G. Seabra, I. Kolossváry, K. F. Wong, F. Paesani, J. Vanicek, J. Liu, X. Wu, S. R. Brozell, T. Steinbrecher, H. Gohlke, Q. Cai, X. Ye, J. Wang, M.-J. Hsieh, G. Cui, D. R. Roe, D. H. Mathews, M. G. Seetin, C. Sagui, V. Babin, T. Luchko, S. Gusarov, A. Kovalenko and P. A. Kollman, *AMBER 11*, University of California, San Francisco, 2010.
78. P. A. Kollman, I. Massova, C. Reyes, B. Kuhn, S. Huo, L. Chong, M. Lee, T. Lee, Y. Duan, W. Wang, O. Donini, P. Cieplak, J. Srinivasan, D. A. Case and T. E. Cheatham III, *Acc. Chem. Res.*, 2000, **33**(12), 889.
79. R. Sijbesma, G. Srdanov, F. Wudl, J. A. Castoro, W. Q. Charles, S. H. Friedman, D. L. Decamp and G. L. Kenyon, *J. Am. Chem. Soc.*, 1993, **115**, 6506.
80. R. Sijbesma, G. Srdanov, F. Wudl, J. A. Castoro, W. Q. Charles, S. H. Friedman, D. L. Decamp and G. L. Kenyon, *J. Am. Chem. Soc.*, 1993, **115**, 6510.
81. S. Durdagi, T. Mavromoustakos, N. Chronakis and M. G. Papadopoulos, *Bioorg. Med. Chem.*, 2008, **16**, 9957.
82. D. Martin and M. Karelson, *Lett. Drug Des. Discovery*, 2010, **7**, 587.
83. H. Tzoupis, G. Leonis, S. Durdagi, M. G. Papadopoulos, V. Bouhllis and T. Mavromoustakos, *J. Comput.-Aided Mol. Des.*, 2011, **25**, 959.
84. S. Durdagi, T. Mavromoustakos and M. G. Papadopoulos, *Bioorg. Med. Chem. Lett.*, 2008, **18**, 6283.
85. S. Durdagi, C. T. Supuran, A. T. Strom, N. Doostdar, M. K. Kumar, A. R. Barron, T. Mavromoustakos and M. G. Papadopoulos, *J. Chem. Inf. Model.*, 2009, **49**, 1139.
86. E. Rutenber, E. B. Fauman, R. J. Keenan, S. Fong, P. S. Furth, P. R. Ortiz de Montellano, E. Meng, I. D. Kuntz, D. L. DeCamp, R. Salto, J. R. Ros, C. S. Craik and R. M. Stroud, *J. Biol. Chem.*, 1993, **268**, 15343.
87. J. Yang and A. R. Barron, *Chem. Commun.*, 2004, 2884.
88. J. Yang, L. B. Alemany, J. Driver, J. Yang and A. R. Barron, *Chem.–Eur. J.*, 2007, **13**, 2530.
89. S. H. Friedman, P. S. Ganapathi, Y. Rubin and G. L. Kenyon, *J. Med. Chem.*, 1998, **41**, 2424.
90. I. Morita, *Prostaglandins Other Lipid Mediators*, 2002, **68–69**, 165–175.
91. B. Samuelsson, *Am. J. Respir. Crit. Care Med.*, 2000, **161**(2), S2–S6.
92. H. Sheng, J. Shao, J. D. Morrow, R. D. Beauchamp and R. N. DuBois, *Cancer*, 10
93. M. Cuendet and J. M. Pezzuto, *Drug Metabol. Drug Interact.*, 2000, **17**, 109.
94. A. J. Dannenberg and K. Subbaramaiah, *Cancer Cell.*, 2003, **4**, 431.
95. T. Mavromoustakos, P. Moutevelis-Minakakis, C. G. Kokotos, P. Kontogianni, A. Politi, P. Zoumpoulakis, J. Findlay, A. Cox, A. Balmforth, A. Zoga and E. Iliodromitis, *Bioorg. Med. Chem.*, 2006, **14**, 4353.

96. W. Sneader, in *Drug Discovery: A History*, John Wiley & Sons, West Sussex, 2005, p. 68.
97. M. G. Malkowski, S. L. Ginnell, W. L. Smith and R. M. Garavito, *Science*, 2000, **289**, 1933.
98. N. Neophytou, G. Leonis, N. Stavrinoudakis, M. Simčič, S. Golič Grdadolnik, E. Papavassilopoulou, G. Michas, P. Moutevelis-Minakakis, M. G. Papadopoulos, M. Zing and T. Mavromoustakos, *Mol. Inf.*, 2011, **30**, 473.
99. G. D. Hawkins, C. J. Cramer and D. G. Truhlar, *J. Phys. Chem.*, 1996, **100**, 19824.
100. J. M. Wood, J. L. Stanton and K. G. Hofbauer, *J. Enzyme Inhib. Med. Chem.*, 1987, **1**, 169.
101. N. A. Powell, F. L. Ciske, C. Cai, D. D. Holsworth, K. Mennen, C. A. Van Huis, M. Jalaie, J. Day, M. Mastronardi, P. McConnell, I. Mochalkin, E. Zhang, M. J. Ryan, J. Bryant, W. Collard, S. Ferreira, C. Gu, R. Collins and J. J. Edmunds, *Bioorg. Med. Chem.*, 2007, **15**, 5912.
102. M. Paul, A. Poyan Mehr and R. Kreutz, *Physiol. Rev.*, 2006, **86**, 747.
103. A. P. Politi, S. Durdagi, P. M. Minakakis, T. Mavromoustakos and G. Kokotos, *J. Mol. Graph. Model.*, 2010, **29**, 425.
104. A. R. Leach, in *Molecular Modelling: Principles and Applications*, Pearson Education Ltd, Essex, 2nd edn, 2001.
105. J. A. Staessen, Y. Li and T. Richart, *Lancet*, 2006, **368**(9545), 1449.
106. M. J. Brown, *Circulation*, 2008, **118**, 773.
107. A. Gradman, R. Schmieder, R. Lins, J. Nussberger, Y. Chiang and M. Bedigian, *Circulation*, 2005, **111**(8), 1012.
108. J. M. Wood, J. Maibaum, J. Rahuel, M. G. Grütter, N. C. Cohen, V. Rasetti, H. Rüger, R. Göschke, S. Stutz, W. Fuhrer, W. Schilling, P. Rigollier, Y. Yamaguchi, F. Cumin, H. P. Baum, C. R. Schnell, P. Herold, R. Mah, C. Jensen, E. O'Brien, A. Stanton and M. P. Bedigian, *Biochem. Biophys. Res. Commun.*, 2003, **308**(4), 698.
109. J. Nussberger, G. Wuerzner, C. Jensen and H. R. Brunner, *Hypertension*, 2002, **39**, e1.
110. I. Stoica, S. K. Sadiq and P. V. Coveney, *J. Am. Chem. Soc.*, 2008, **130**, 2639.
111. T. Hou, J. Wang, Y. Li and W. Wang, *J. Chem. Inf. Model.*, 2011, **51**, 69.
112. M. Lucio, J.L.F.C. Lima and S. Reis, *Curr. Med. Chem.*, 2010, **17**, 1795.
113. A. M. Seddon, D. Casey, R. V. Law, A. Gee and R. H. Templer, *O. Ces, Chem. Soc. Rev.*, 2009, **38**, 2509.
114. T. Mavromoustakos, P. Zoumpoulakis, I. Kyrikou, A. Zoga, E. Siapi, M. Zervou, I. Daliani, D. Dimitriou, A. Pitsas, C. Kamoutsis and P. Laggner, *Curr. Top. Med. Chem.*, 2004, **4**, 445.
115. J. K. Seydel, M. A. Velasco, E. A. Coats, H. P. Cordes, B. Kunz and M. Wiese, *Quant. Struct.-Act. Relat.*, 1992, **11**, 205.
116. D. A. Middleton, *Annu. Rep. NMR Spectrosc.*, 2007, **60**, 39.

117. J. K. Seydel and M. Wiese, *Drug–Membrane Interactions: Analysis, Drug Distribution, Modeling*, Wiley-VCH Verlag GmbH & Co., Weinheim, 2002.
118. T. Mavromoustakos, *The Use of Differential Scanning Calorimetry to Study Drug-Membrane Interactions*, Methods in Molecular Biology, Methods in Membrane Lipids, ed. A. M. Dopico, Humana Press Inc., Tuttowas, NJ, 2008, vol. 400, ch. 39, pp. 587–600 (other articles are related to other methodologies).
119. X. L. Liu, P. Fan, M. Chen, H. Hefesha, G. K. E. Scriba, D. Gabel and A. Fahr, *Helv. Chim. Acta*, 2010, **93**, 203.
120. M. Carini, G. Aldini, G. M. Orioli and M. R. M. Facino, *Curr. Pharm. Anal.*, 2006, **2**, 141.
121. T. Mavromoustakos, D. P. Yang, A. Charalambous, L. G. Herbette and A. Makriyannis, *Biochim. Biophys. Acta*, 1990, **1024**, 336.
122. T. Mavromoustakos, D. P. Yang, W. Broderick, D. Fournier, L. G. Herbette and A. Makriyannis, *Pharmacol. Biochem. Behav.*, 1991, **40**, 547.
123. D. W. Chester, V. Skita, H.S. Young, T. Mavromoustakos and P. Shrittmatter, *Biophys. J.*, 1992, **61**, 1224.
124. D. P. Yang, T. Mavromoustakos, K. Beshah and A. Makriyannis, *Biochim. Biophys. Acta*, 1992, **1103**, 25. 11
125. D. P. Yang, T. Mavromoustakos and A. Makriyannis, *Life Sci.*, 1993, **53**, 117.
126. M.A. Makriyannis, T. Mavromoustakos, K. Kelly and K. R. Jeffrey, *Biochim. Biophys. Acta*, 1993, **1151**, 51.
127. T. Mavromoustakos, D. P. Yang and A. Makriyannis, *Biochim. Biophys. Acta*, 1994, **1194**(1), 69.
128. T. Mavromoustakos, D. P. Yang and A. Makriyannis, *Biochim. Biophys. Acta*, 1995, **1237**, 183.
129. T. Mavromoustakos, D. P. Yang and A. Makriyannis, *Biochim. Biophys. Acta*, 1995, **1239**(2), 257.
130. T. Mavromoustakos, E. Theodoropoulou, D. Papahatjis, T. Kourouli, D. P. Yang, M. Trumbore and A. Makriyannis, *Biochim. Biophys. Acta*, 1996, **1281**(2), 235.
131. M. Koufaki, T. Calogeropoulou, T. Mavromoustakos, E. Theodoropoulou, A. Tsoinis and A. Makriyannis, *J. Heterocycl. Chem.*, 1996, **33**, 619.
132. T. Mavromoustakos, D. P. Yang and A. Makriyannis, *Life Sci.*, 1996, **59**(23), 1969.
133. T. Mavromoustakos, E. Theodoropoulou, C. Dimitriou, J. Matsoukas, D. Panagiotopoulos and A. Makriyannis, *Lett. Pept. Sci.*, 1996, **3**(4), 175.
134. T. Mavromoustakos, E. Theodoropoulou and D. P. Yang, *Biochim. Biophys. Acta*, 1997, **1328**(1), 65.
135. T. Mavromoustakos, A. Papadopoulos, E. Theodoropoulou, C. Dimitriou and E. A. Byza, *Life Sci.*, 1998, **62**(20), 1901.
136. T. Mavromoustakos and E. Theodoropoulou, *Chem. Phys. Lipids*, 1998, **92**(1), 37.

137. T. Mavromoustakos, D. Papahatjis and P. Laggner, *Biochim. Biophys. Acta*, 2001, **1512**(2), 183.
138. H. Maswadeh, C. Demetzos, I. Daliani, I. Kyrikou, T. Mavromoustakos, A. Tsortos and G. Nounesis, *Biochim. Biophys. Acta*, 2002, **1567**, 49.
139. I. Kyrikou, I. Daliani, T. Mavromoustakos, H. Maswadeh, C. Demetzos, S. Xatziantoniou, S. Giatrellis and G. Nounesis, *Biochim. Biophys. Acta*, 2004, **1661**, 1.
140. I. Kyrikou, S. Xadjikakou, D. Kovala-Demertzi, K. Viras and T. Mavromoustakos, *Chem. Phys. Lipids*, 2004, **132**, 157.
141. I. Kyrikou, T. Mavromoustakos, S. Xatziantoniou, A. Georgopoulos and C. Demetzos, *Chem. Phys. Lipids*, 2005, **133**, 125.
142. N.-P. Benetis, I. Kyrikou, T. Mavromoustakos and M. Zervou, *Chem. Phys.*, 2005, **314**(1–3), 57.
143. V. Saroglou, S. Xatziantoniou, M. Smyrniotakis, I. Kyrikou, T. Mavromoustakos, A. Zompra, V. Magafa, P. Cordopatis and C. Demetzos, *J. Pept. Sci.*, 2006, **12**, 43.
144. C. Koukoulitsa, I. Kyrikou, C. Demetzos and T. Mavromoustakos, *Chem. Phys. Lipids*, 2006, **144**, 85.
145. I. Kyrikou, C. Poulos, N. Benetis, K. Viras, M. Zervou and T. Mavromoustakos, *Biochim. Biophys. Acta*, 2008, **1778**, 113.
146. C. Koukoulitsa, S. Durdagi, E. Siapi, C. Villalonga-Barber, X. Alexi, B. R. Steele, M. Micha-Screttas, M. N. Alexis, A. Kakoulidou and T. Mavromoustakos, *Eur. Biophys. J.*, 2011, **40**, 865.
147. P. Zoumpoulakis, I. Daliani, M. Zervou, I. Kyrikou, E. Siapi, G. Lamprinidis, E. Mikros and T. Mavromoustakos, *Chem. Phys. Lipids*, 2003, **125**, 13.
148. C. Fotakis, S. Gega, E. Siapi, C. Potamitis, K. Viras, P. Moutevelis-Minakakis, G. Kokotos, S. Durdagi, S. Grdadolnik, B. Sartori, M. Rappolt and T. Mavromoustakos, *Biochim. Biophys. Acta*, 2010, **1798**(3), 422.
149. T. Mavromoustakos, P. Chatzigeorgiou, C. Koukoulitsa and S. Durdagi, *Int. J. Quantum Chem.*, 2011, **6**, 1172.
150. C. Potamitis, P. Chatzigeorgiou, E. Siapi, T. Mavromoustakos, A. Hodzic, F. Cacho-Nerin, P. Laggner and M. Rappolt, *Biochim. Biophys. Acta*, 2011, **1808**, 1753.
151. C. Fotakis, D. Christodouleas, P. Zoumpoulakis, A. Gili, E. Kritsi, N.-P. Benetis, M. Zervou, H. Reis, M. G. Papadopoulos and T. Mavromoustakos, *J. Chem. Phys. B*, 2011, **115**, 6180.
152. D. Ntountaniotis, G. Mali, S. G. Grdadolnik, M. Halabalaki, A.-L. Skaltsounis, C. Potamitis, E. Siapi, P. Chatzigeorgiou, M. Rappolt and T. Mavromoustakos, *Biochim. Biophys. Acta*, 2011, **1808**, 2995.
153. T. Mavromoustakos, S. Durdagi, C. Koukoulitsa, M. Simcic, M. G. Papadopoulos, M. Hodoscek and S. G. Grdadolnik, *Curr. Med. Chem.*, 2011, **18**, 2517.
154. T. Mavromoustakos, P. Moutevelis-Minakakis, G. Kokotos, E. Papavassilopoulou, C. Potamitis, C. Fotakis, P. Chatzigeorgiou, K. Vyras,

- C. Koukoulitsa, E. Kalatzis and S. Durdagi, Peptide mimetics drugs and their interdigitation with lipid bilayers, in *Essays on Contemporary Peptide Science*, ed. P. Cordopatis, Research SignPost, 2011, ch. 6, pp. 95–113. ISBN: 978-81-308-0428-6. 12
155. L. J. Wagenaar, A. A. Voors, H. Buikema, A. van Buiten, R. H. Luubeck, P. W. Boonstra, D. J. van Veldhuisen and W. H. van Gilst, *Cardiovasc. Drugs Ther.*, 2002, **16**, 311.
156. T. Unger, *Eur. Heart J. Suppl.*, 2004, **6**, H11.

Authors Queries

Journal: **Towards Efficient Designing of Safe Nanomaterials: Innovative Merge of Computational Approaches and Experimental Techniques**

Paper:

Title: **Theoretical Studies of Interactions in Nanomaterials and Biological Systems**

Dear Author

During the preparation of your manuscript for publication, the questions listed below have arisen. Please attend to these matters and return this form with your proof. Many thanks for your assistance

Query Reference	Query	Remarks
1	In Table 8.5, please check the columns have been displayed correctly, and the basis sets in the footnotes.	
2	In Figure 8.3, the dashed lines in the top figure appear to be solid – please resupply the image.	
3	Please define the xc-potential for the reader.	
4	In the sentence beginning ‘Thus, these inhibition data...’ is there a verb missing after ‘assist in’, perhaps ‘assist in processing’?	
5	Ref. 103 is not currently cited in the text – please indicate a location for the citation.	
6	The citation to Figure 8.7b has been changed to Figure 8.8b to match the text – please check this is correct.	

7	The sentence beginning 'Thanks to advances in...' has been altered for clarity – please check the meaning has not been affected.	
8	The resolution of Figure 8.9 appears to be low – please resupply at >300 dpi.	
9	The page number has been corrected in ref. 18 – please check.	
10	Please provide the year and the volume and page numbers for ref. 92.	
11	The CASSI journal abbreviation has been added to ref. 124, 126–130, 134, 137–139 – please check the references are correct.	
12	Please provide the publisher's location for ref. 154.	